Zhong *et al. Biology Direct* (2026) 21:76
https://doi.org/10.1186/s13062-026-00779-3

Biology Direct

RESEARCH Open Access

An integrated microbiome-drug interaction and bioinformatics approach identifies active deglycosylated and glycosidic chain metabolites of Platycodin D targeting PTPN2/HIF1A in acute lung injury

Yuanhan Zhong[1,2†], Yu Peng[1,2†], Shouwen Zhang[1,2†], Liyun Wen[1,2], Guangpeng Liu[1,2], Bingbing Xu[3], Yonghong Liang[1,2], Huiliang Huang[1,2], Junwei He[1,2], Yong Feng[4], Jinxiang Zeng[1,2*] and Jian Liang[1,2*]

Abstract

Background Platycodin D (PD) is a typical triterpenoid saponin with low oral bioavailability. Despite its potent anti-ALI effects, its active metabolites and underlying mechanisms remain unclear, thereby significantly impeding its further development. This study aimed to establish a new integrated method combining microbiome-drug interaction analysis, bioinformatics approaches, and experimental validation to elucidate the active metabolites and mechanisms by which PD exerts anti-ALI effects.

Methods Microbiome-drug interaction analysis identified PD-derived metabolites, including deglycosylated metabolites (DGMs), glycosidic chain metabolites (GCMs), and short-chain fatty acids (SCFAs) derived from the glycosidic chains, while simultaneously assessing PD's modulatory effects on the intestinal microbiota. Bioinformatics approaches predicted the potential anti-ALI targets of the metabolites in the blood. The bioactivities and mechanisms of these metabolites were subsequently validated using LPS-induced and pseudo-sterile ALI mouse models and molecular docking.

Results PD and its 9 DGMs were identified in vitro, while only Deapio-platycodin D (DPD), 3-O-β-D-glucopyranosyl platycodigenin (GPN) and platycodigenin (PN) were detected in serum; 9 GCMs including 1 trisaccharide, 2 disaccharides and 5 monosaccharides derived from the glycosidic chain of PD were identified in vitro. Only 5 monosaccharides of Glucose (Glu), Arabinose (Ara), Rhamnose (Rha), Xylose (Xyl) and Apiose (Api) were detected in serum. Notably, saccharide-to-SCFA transformation was markedly inhibited both in vitro and in serum. PD also

†Yuanhan Zhong, Yu Peng and Shouwen Zhang contributed equally to this work.

*Correspondence:
Jinxiang Zeng
zjx@jxutcm.edu.cn
Jian Liang
ocean719@163.com

Full list of author information is available at the end of the article

modulated intestinal microbiota by increasing probiotics and reducing pathogens. Bioinformatics analysis showed DGMs targeted PTPN2, whereas GCMs co-targeted both PTPN2 and HIF1A. In vivo models confirmed the activities and mechanisms of PD, while molecular docking further verified the active metabolites were 2 DGMs of GPN, PN and 5 GCMs of Glu, Ara, Rha, Xyl and Api.

Conclusions Novel active metabolites and mechanisms of PD against ALI were elucidated and validated by the proposed strategy. Bioactivity of PD extends beyond its metabolites with parent nucleus, as GCMs of PD also showed significant activities. SCFAs are not necessarily active metabolites of PD despite its saccharide-rich structures. In addition, this study establishes a new paradigm for elucidating active metabolites and mechanisms of glycosides, especially those with low oral bioavailability, advancing natural product-based ALI treatment strategies.

Keywords Platycodin D, Microbiome-drug interaction, Bioinformatics analysis, Acute lung injury, Active metabolite; mechanism of action

Introduction

Acute lung injury (ALI) is an acute diffuse pulmonary inflammation caused by factors such as infection, inhalation of harmful substances, trauma, or shock. In severe cases, it progresses to acute respiratory distress syndrome, characterized by dysregulation of pulmonary inflammation, increased vascular permeability, and respiratory failure [1]. Globally, approximately 3 million patients are affected annually, with an extremely high mortality rate: 30–40% in high-income regions and over 50% in resource-limited settings [2], imposing a huge global burden. The pathogenesis of ALI is complex, including inflammatory dysregulation, cytokine storm and disruption of the alveolar-capillary barrier, which poses severe challenges to clinical treatment. Current clinical management relies on supportive care such as pulmonary mechanical ventilation, and there is no effective drug treatment to change the disease progression [2]. Although glucocorticoids are usually used as first-line drugs, systematic reviews have confirmed that they have no significant impact on the mortality rate of patients, and long-term use may lead to serious complications [3]. This severe therapeutic gap has become more urgent in the post COVID-19 era [4].

Numerous natural products are employed for the treatment of ALI, demonstrating both safety and efficacy [5], including flavonoid glycosides, saponins, iridoid glycosides, coumarin glycosides and anthraquinone glycosides, which are from a large family of glycosidic components. However, even though they possess good bioactivities [6, 7], most of them were disregarded in further therapeutic development due to poor oral bioavailability [6]. Increasing evidence in the past decade shows that, after oral administration, natural products always undergo extensive structural modification by the intestinal microbiota before systemic absorption, generating metabolites with enhanced bioavailability and activity [6]. Thus, active metabolites, especially for those with low oral bioavailability, rather than prototypes alone, may account for therapeutic efficacy [6, 7]. Such metabolites themselves can be developed as lead compounds [8]. In addition, natural products can beneficially modulate intestinal microbial composition [9, 10]. On the other hand, the key approach to studying the complex bidirectional interactions between natural products and the intestinal microbiota lies in microbiome-drug interaction analysis [11, 12]. Therefore, studying the active metabolites of natural products with anti-ALI effects and their impact on the intestinal microbiota based on microbiota-drug interactions is of great significance for the development of new natural product-based anti-ALI drugs [11, 12]. Nevertheless, most prior studies emphasize aglycone-retaining metabolites, while glycosidic chain-derived monosaccharides or oligosaccharides and SCFAs remain relatively neglected.

Beyond microbiome-drug interaction analysis, bioinformatics offers indispensable computational tools to analyze complex biological data and complement experimental findings. Techniques such as Weighted Gene Co-expression Network Analysis (WGCNA) construct co-expression networks based on actual transcriptomic data, identifying functionally related gene modules and hub genes highly correlated with phenotypes. This data-driven approach, when integrated with multi-database target prediction for specific metabolites, establishes a more robust and biologically relevant framework for identifying potential therapeutic targets. This significantly reduces false positives compared to traditional methods, making it particularly well-suited for elucidating the complex, multi-target mechanisms of natural product metabolites [13, 14].

Platycodon grandiflorum(Jacq.) A.D is a traditional edible-medicinal plant used for respiratory disorders. Its therapeutic activities correlate with platycoside saponins, among which PD is the most abundant [15]. Structurally, PD possesses an oleane-type pentacyclic triterpene parent nucleus, whose C-3 position and C-28 positions are linked with a saccharide chains consisting of glucose (Glu), arabinose (Ara), rhamnose (Rha), xylose (Xyl), and apiose (Api), contributing to its low oral bioavailability

[16] yet strong anti-ALI efficacy [17, 18]. Recent studies show that it is difficult for PD to spontaneously bind with targets to exert its effects; microbiota-derived DGMs display enhanced bioactivity [19, 20]. Oligosaccharides and monosaccharides can also be biologically active [21–23] and are reported to yield SCFAs after further microbial fermentation [24]. Collectively, this suggests that the glycosidic chain metabolites (GCMs), namely the oligosaccharides and monosaccharides of PD, will inevitably be produced during the deglycosylation metabolism. These compounds could all contribute to PD's anti-ALI effect.

This study employed microbiome-drug interaction analysis to reveal the bidirectional interaction between PD and the intestinal microbiota. Subsequently, bioinformatics approaches were used to predict the potential targets of PD metabolites against ALI. Then, LPS-induced and pseudo-sterile mouse models were applied to verify the activities and mechanisms of PD in the treatment of ALI; and molecular docking were applied to verify its active metabolites. The results showed that the new method integrating microbiome-drug interaction analysis, bioinformatics approaches and experimental verification, could successfully reveal the novel active metabolites and the mechanism of PD in treating ALI.

Methods

Study design

A multi-tier investigation comprising: (1) in vitro anaerobic incubation of PD with murine intestinal microbiota; (2) serum pharmacochemistry after oral PD administration in LPS-induced ALI mice; (3) bioinformatics integration (DEGs + WGCNA from two GEO ALI datasets) intersected with in silico target prediction; (4) functional validation in LPS-induced ALI and pseudo-sterile (antibiotic-depleted microbiota) mouse models; (5) mechanistic protein analyses; (6) molecular docking; (7) 16S rRNA sequencing to define reciprocal microbiota modulation.

Drugs and reagents

PD and Deapio-platycodin D (DPD) were purchased from MUST Bio-technology Co., Ltd (Chengdu, China). 3-O-β-D-glucopyranosyl platycodigenin (GPN), and platycodigenin (PN), Glucose (Glu), Arabinose (Ara), Rhamnose (Rha), Xylose (Xyl) and Apiose (Api) were purchased from Yuanye Bio-Technology Co., Ltd (Shanghai, China). Acetic acid, propionic acid, butyric acid, isobutyric acid, 2-methylbutyric acid, isovaleric acid, valeric acid, hexanoic acid, 4-methylvaleric acid and ^{13}C6-Glucose were purchased from Maclean Biochemical Technology Co., Ltd (Shanghai, China). The purity of all the standard substances mentioned above is greater than 98%. General anaerobic medium (GAM) for microbiota biotransformation was purchased from Haibo biotechnology Co., Ltd. (Qingdao, China). ELISA kits for detecting IL-1β, IL-6 and TNF-α were purchased from HUABIO Biotechnology Co., Ltd. (Hangzhou, China). The primary antibodies of phospho-epidermal growth factor receptor (p-EGFR), epidermal growth factor receptor (EGFR), phospho-tyrosine-protein kinase JAK1 (p-JAK1), tyrosine-protein kinase JAK1 (JAK1), hypoxia-inducible factor 1 A (HIF1A) and β-actin were purchased from Abcam (Cambridge, UK), the primary antibodies of phospho-signal transducer and activator of transcription 3 (p-STAT3), signal transducer and activator of transcription 3 (STAT3) and Lamin B1 were purchased from HUABIO Biotechnology Co., Ltd. (Hangzhou, China), and the primary antibody of tyrosine-protein phosphatase non-receptor type 2 (PTPN2) was purchased from Thermo Fisher Scientific (Waltham, MA, USA). The secondary antibody was purchased from Cell Signaling Technology (Danvers, MA, USA).

Animals

SPF male BALB/c mice (6–8 weeks old; 20–22 g) were purchased from Hunan Slite Jingda Experimental Animal Co., Ltd (license No. SCXK(Xiang) 2021–0002). Male BALB/C mice were used in this study to minimize experimental variability associated with estrous cycles and hormonal fluctuations in female mice, which is a common practice in studies focusing on intestinal microbial metabolism and in vivo pharmacological evaluation. The mice were housed in an SPF facility under controlled conditions (temperature 23–27 °C; humidity 50–60%) with ad libitum access to standard chow and water on a 12-hour light/dark cycle. They were acclimated for one week prior to experimentation. All procedures complied with institutional and national guidelines for the care and use of laboratory animals and were approved by the Animal Care and Use Committee of Jiangxi University of Chinese Medicine (approval No. JZLLSC20250550).

Methods for microbiome-drug interaction analysis

In vitro biotransformation of PD by intestinal microbiota

After 7 days of acclimatization, an ALI mouse model was established in 12 male BALB/c mice via intratracheal instillation of LPS (5 mg/kg). 12 hours after tracheal instillation, the feces of mice were collected for in vitro biotransformation experiments. Intestinal microbiota isolation procedure was performed following established protocols with minor modifications [20, 25]. Briefly, 9.5 g GAM medium was dissolved in 1000 mL of deionized water and autoclaved at 121 °C under 0.15 MPa pressure for 30 min. Fresh feces were collected from Balb/c mice and immediately homogenized with sterile normal saline at a 1:4 (w/v) ratio using a vortex mixer. The homogenate was centrifuged at 1,000 rpm for 10 min remove fecal particles. GAM was added to the supernatant at a ratio of 9:1 (v/v), vortexed and mixed to obtain the

intestinal bacteria culture medium. The experiment was divided into two groups: a blank control group of intestinal bacteria and a PD group. The blank control group was composed of intestinal bacteria culture medium, and PD group was composed of intestinal bacteria culture medium and PD (final concentration 0.2 mg/mL, from a 2 mg/mL stock solution). The samples were anaerobically cultured at 37 °C for 0, 1, 2, 4, 6, 12, 24 and 48 h. At each incubation time point, equal volumes of culture medium from three independent culture flasks were combined and thoroughly mixed. After incubation, three volumes of methanol were added to precipitate the proteins in the medium, the mixture was centrifuged at 14,000 rpm for 20 min, and the supernatant was collected for subsequent experiments.

Preparation of DGMs samples of PD in vitro

The extraction of DGMs was performed according to our previous methodology [25, 26]. Briefly, after vacuum drying, 200 µL of supernatant of the cultured sample or mixed standard solution of platycosides (PD, 1.4 mg/mL; DPD, 1.9 mg/mL; GPN, 1.4 mg/mL; PN, 0.7 mg/mL) was redissolved in 200 µL of n-butanol saturated water. An equal amount of water-saturated n-butanol was then added for liquid-liquid extraction; this step was repeated three times. The organic phases were combined and dried under vacuum, then redissolved in 200 µL of methanol. The final samples for UHPLC-LTQ-Orbitrap MS analysis were centrifuged at 14,000 rpm for 20 min before MS analysis.

Preparation of GCMs samples of PD in vitro

The GCMs of PD were analyzed by pre-column derivatization with 1-phenyl-3-methyl-5-pyrazolinone (PMP) [27]. To 200 µL of the supernatant of the incubated intestinal bacteria culture solution was added with 50 µL of 5 µg/mL ^{13}C6-Glucose solution (internal standard), and 50 µL of methanol was added to the mixed standard solution (Glu, 0.43 mg/mL; Ara, 0.35 mg/mL; Rha, 0.36 mg/mL; Xyl, 0.30 mg/mL; Api, 0.32 mg/mL). Subsequently, the sample was dried under vacuum and redissolved in 200 µL of ammonium hydroxide. Then 200 µL of 0.3 M PMP solution was added; the mixture was mixed well and reacted at 70 °C for 30 min. After the reaction, 2 mL of methanol was added and the mixture was dried under vacuum. This procedure was repeated three times to remove ammonium hydroxide. The mixture was redissolved in 200 µL of deionized water, then extracted three times with equal volumes of chloroform. The extracted water phase was centrifuged at 14,000 rpm for 20 min and then used for UHPLC-LTQ-Orbitrap MS analysis.

Preparation of SCFAs samples of PD in vitro

Pre-column derivatization with 3-nitrophenylhydrazine (3-NPH) was used to analyze the SCFAs in the culture medium of intestinal microbiota [28]. To 200 µL of the supernatant of the incubated intestinal bacteria culture solution was added with 50 µL of 5 µg/mL 4-methylvaleric acid solution (internal standard). 100 µL of methanol was added to the mixed standard solution (acetic acid, 1.05 mg/mL; propionic acid, 0.99 mg/mL; isobutyric acid, 0.95 mg/mL; butyric acid, 0.96 mg/mL; 2-methylbutyric acid, 0.94 mg/mL; isovaleric acid, 0.93 mg/mL; valeric acid, 0.94 mg/mL; hexanoic acid, 0.93 mg/mL). Subsequently, the sample was dried under vacuum, then redissolved in 200 µL of methanol. Then, 100 µL of a 7% pyridine methanol solution, 100 µL of a 50 mM 1-ethyl-3-(3-dimethylaminopropyl) carbodiimide (EDC) methanol solution, and 100 µL of a 50 mM 3-NPH methanol solution were added. After mixing, the reaction was conducted at 37 °C for 30 min. Following the reaction, the solution was dried under vacuum, then redissolved in 200 µL of deionized water, and then extracted with an equal volume of methyl tert-butyl ether (MTBE). This extraction was repeated three times. All the MTBE phases were dried and redissolved in 200 µL of methanol, centrifuged at 14,000 rpm for 20 min, and then used for UHPLC-LTQ-Orbitrap MS analysis.

Analysis of the blood-absorbed PD metabolites in serum

12 hours after LPS-induced ALI in mice, 12 male BALB/C mice were allowed free access to water but fasted for 12 hours. Then 6 mice were orally administered 400 mg/kg of PD, while the remaining 6 mice were administered the same amount of normal saline. 0.1 mL of blood sample was collected from the retroorbital venous plexus of each mouse at 0, 1, 2, 4, 6, and 12 h after dosing via retro-orbital sampling performed under anesthesia by experienced personnel, followed by hemostasis and close monitoring to minimize pain and distress. Equal volumes of the collected blood samples from three individuals at each time point were thoroughly mixed and then centrifuged at 3,500 rpm at 4 °C for 10 min. The supernatant was collected to obtain the serum containing the PD metabolites. To precipitate the proteins, three times the volume of methanol was added to the serum. After centrifugation at 14,000 rpm for 20 min (4℃), the protein-free serum sample was obtained. Subsequently, the methods for extracting DGMs of PD from serum and the pre-column derivatization analysis methods for GCMs and SCFAs in serum were consistent with the analysis methods in vitro.

Chromatographic and mass spectrometric conditions

The analysis of PD metabolites, both in vitro and in serum, was performed using an LTQ-Orbitrap MS^{n}mass

spectrometer equipped with an Ultmate 3000 Binary RSLC system (Thermo Fisher Scientific, Waltham, MA, USA). The chromatographic separation of metabolites was performed on a ZORBAX RRHD Eclipse Plus C18 column (100 mm × 2.1 mm, 1.8 μm, Agilent Technologies, California, USA). The mobile phase consisted of 0.1% formic acid aqueous solution (A, v/v) and acetonitrile (B). The analysis conditions for the DGMs of PD, both in vitro and in serum, were the same, which were consistent with the analysis method used in our previous study [19, 26]. The separation conditions are as follows: 0–30 min, 15% B; 30–45 min, 15% –24% B; 45–62 min, 24% –71% B; 62–67 min, 71% –95% B; 67–68 min, 95% –15% B; 68–70 min, 15% B. Chromatographic separation was performed at 40 °C with an injection volume of 4 μL and a flow rate of 0.3 mL/min. The analysis conditions for the GCMs of PD in vitro and in serum were the same, with the following gradient conditions: 0–2 min, 15%-17% B; 2–18 min, 17%-23% B; 18–21 min, 23%-100% B; 21–23 min, 100% B; 23–24 min, 100%-15% B; 24–25 min, 15% B. The column temperature was 40 °C, the injection volume was 4 μL, and the flow rate was 0.25 mL/min. The separation conditions for the SCFAs of PD in vitro and in serum are the same: 0-2 min, 15% –17% B; 2–19 min, 20% –43% B; 19–22 min, 43% B; 22–22.1 min, 43% –15% B; 22.1–25 min, 15% B. The column temperature was maintained at 40 °C with an injection volume of 4 μL, and a flow rate of 0.25 mL/min.

The data collection of DGMs and SCFAs was carried out in negative ion mode [19, 26, 28], while the data collection of GCMs was carried out in positive ion mode [27]. MS data were acquired in both positive and negative ion modes using an electrospray ion source. MS parameters are as follows: capillary temperature 320 °C, sheath gas flow 35 arb, auxiliary gas flow 10 arb, spray voltage 3.5 and –3.5 kV, capillary voltage 35 and –35 V, tube lens voltage 110 and –110 V, full scan range 50–1,500 Da, detection resolution 30,000. MS^2data was collected in data-dependent scanning mode, selecting the top 6 peaks with the highest abundance in MS^1 for collision-induced dissociation scanning of fragments.

Methods for bioinformatics analysis

Acquisition of targets for PD metabolites in serum

The PubChem database (https://pubchem.ncbi.nlm.nih.gov/) was searched for the standard SDF structure of the metabolite of PD absorbed into blood or drawn by ChemDraw software and then converted to SDF format. Then, by uploading its classic SDF structure to Pharmmapper platform (https://lilab-ecust.cn/pharmmapper/), SwissTargetPrediction platform (http://swisstargetprediction.ch/), and Super-PRED database (https://prediction.charite.de/), possible targets could be identified based on the two-dimensional and three-dimensional similarity of the predicted ligand can be found.

Dataset acquisition and analysis of differentially expressed genes (DEGs) of ALI

Datasets GSE2411 and GSE18341 were obtained from Gene Expression Omnibus (GEO) database (https://www.ncbi.nlm.nih.gov/geo/). The GSE2411 dataset includes expression data from lung tissues of 6 mice stimulated by LPS and 6 mice as normal control group. The GSE18341 dataset contains expression data from lung tissues of 8 mice stimulated by LPS and 8 normal mice. The GSE2411 dataset annotates the microarray dataset according to the gene ID provided by GPL339 platform information, and the GSE18341 dataset annotates the microarray dataset according to GPL1261. The "Limma" package in R software (version 4.4.1) was used for differential expression genes (DEGs) analysis. The screening criteria for DEGs were log2FC value < –1 or log2FC > 1, with an adjusted p-value < 0.05. The corresponding volcano plots were drawn using the "ggplot2" package in R software. Subsequently, the DEGs from the two datasets were extracted, duplicate values were removed respectively, and a Venn diagram was made to find the intersection of the two datasets.

Construction of WGCNA of ALI

Gene co-expression network construction and identification of key genes significantly associated with ALI were performed using the "WGCNA" package (R version 4.4.1). Input genes were selected as the top 25% of genes with the highest median expression values from the expression profile. First, the "pick Soft Threshold" function was employed to determine an appropriate soft-thresholding power (β). A scale-free topology fit index (R^2) of 0.85 was targeted, and the corresponding βvalue was chosen to establish a scale-free topological model. Subsequently, a hierarchical clustering tree was constructed based on the topological overlap matrix (TOM), and genes with similar expression patterns were grouped into distinct modules, each containing a minimum of 100 genes. Finally, gene significance (GS) for ALI and module membership (MM) within each hub module were calculated. Hub genes within these modules were defined as those meeting the stringent criteria of GS > 0.90 and MM > 0.90 [29].

Acquisition of targets of PD metabolites for anti-ALI

The DEGs and WGCNA analysis results from the GSE2411 and GSE18341 datasets were intersected to identify the ALI-related targets. The targets of PD DGMs and GCMs were then separately intersected with these ALI-related targets, yielding the core targets mediating the anti-ALI effects of the DGMs and GCMs.

Methods for experimental verification

LPS-induced ALI and pseudo-sterile mouse models

After 7 days of acclimatization, 80 male BALB/c mice were randomly assigned to eight groups ($n = 10$ per group): Control group, LPS group (LPS, 5 mg/kg), Positive control group (dexamethasone, Dex, 5 mg/kg), PD low-dosage group (PD-L, 10 mg/kg), PD medium-dose (PD-M, 20 mg/kg), PD high-dosage group (PD-H, 40 mg/kg), mixed antibiotics group (Abs, containing 100 mg/kg each of vancomycin, ampicillin, metronidazole and neomycin sulfate), and mixed antibiotics and high-dosage PD group (Abs+PD-H, 100 mg/kg mixed antibiotics and 40 mg/kg PD). All groups received daily oral gavage (10 mL/kg) for 7 consecutive days. The normal control and LPS model groups were administered an equivalent volume of distilled water.

On day 13 (24 h prior to the final administration), all mice except the control group were given intratracheal instillation of LPS (5 mg/kg) to induce ALI. The control group received an equal volume of PBS buffer. Before the last gavage, the mice fasted for 12 hours and were allowed to drink water freely. One hour after final administration, blood was collected via retro-orbital sampling performed under anesthesia by experienced personnel, followed by hemostasis and close monitoring to minimize pain and distress. The serum was then separated by centrifugation at 3,500 rpm for 10 min and stored at 4 °C for subsequent analysis. Mice were then sacrificed, and the trachea and lungs were fully exposed. After tracheal cannulation with an intravenous infusion needle, the right hilum was ligated. The left lung was lavaged three times with 0.3 mL of ice-cold PBS per wash. Bronchoalveolar lavage fluid (BALF) was collected. The right upper lung was fixed in 4% paraformaldehyde for histopathology, while the remaining right lung tissue was stored at −80 °C for further assays.

Histopathological features of the lung

Fixed lung tissues (4% paraformaldehyde) were rinsed overnight under tap water. They underwent graded ethanol dehydration (70% – 100%), xylene clearing, and paraffin embedding (56 - 58℃). Sections (4 μm) were cut, baked (60 °C, 2 h), deparaffinized in xylene, and rehydrated through descending ethanol. Nuclei were stained with Harris hematoxylin (5 min), differentiated (0.5% acid alcohol, 30 s), and counterstained with eosin Y (1 min). Sections were dehydrated, cleared in xylene, permanently mounted, and evaluated for alveolar integrity, inflammation, and fibrosis. The histopathological score was completed by professional pathologists. The lung injury score ranges from 0 to 4 points (0 points represent the mildest or extremely mild injury, and 1, 2, 3, and 4 points represent mild, moderate, severe, and maximum injury respectively).

Lung wet/dry weight ratio (W/D)

The lung wet/dry weight ratio (W/D) is a reliable, quantitative, and widely used indicator for assessing the severity of pulmonary edema in ALI models. An increase in this ratio directly reflects elevated pulmonary vascular permeability and fluid leakage, which are key pathophysiological features of ALI. In this study, the right upper lung tissue was harvested from mice, blotted dry with filter paper to remove surface moisture, and its wet weight was measured. Subsequently, the tissue was placed in a constant-temperature oven at 70 °C for 72 hours. Following drying, the dry weight was measured, and the W/D ratio was calculated.

Biochemical indexes measurement

BALF was centrifuged at 3,500 rpm and 4 °C for 10 min. The precipitate was resuspended in 500 μL of PBS and leukocytes were counted with a cytometer, and the supernatant of BALF was used to determine the content of cytokines [17]. According to the manual instructions of the ELISA kit, the contents of IL-1β, IL-6 and TNF-α in serum and BALF were determined.

Western blotting analysis

For Western blotting analysis, lung tissues were homogenized in ice-cold 2% sodium dodecyl sulfate (SDS) lysis buffer (containing 1 mM PMSF) and incubated at 4 °C for 20 min to facilitate complete lysis [19]. After centrifugation (10,000 rpm, 4 °C, 30 min), the supernatant protein concentration was determined by BCA assay. Protein samples were mixed with 5× SDS loading buffer and denatured by heating at 100 °C for 10 min using a metal heating block. Each sample was loaded with 20 μg of denatured protein and subjected to electrophoresis on a 10% SDS-polyacrylamide gel for 90 min at a constant voltage of 100 V. The proteins were transferred onto the PVDF membrane under a constant current (400 mA) for 50 min and blocked with 5% (w/v) skimmed milk. Membranes were probed overnight at 4 °C with primary antibodies: JAK1 (1: 500), p-JAK1 (1: 500), STAT3(1: 1,000), p-STAT3 (1: 1,000), EGFR (1:500), p-EGFR (1: 500), PTPN2 (1:1,000), HIF1A (1: 1,000) and β-actin (1:5,000), and then incubated with an HRP-conjugated secondary antibody (1: 2,000). Finally, the membrane was incubated with an enhanced chemiluminescence kit and analyzed using Image Lab software.

To explore the nuclear translocation of p-STAT3 and HIF1A, specific detections for nuclear proteins were conducted. Nuclear proteins were extracted from lung tissues using a Nuclear/Cytoplasmic Extraction Kit following manufacturer's protocol. After quantification by BCA, the protein was denatured in a metal bath at 100 °C for 10 min and then loaded onto an SDS-polyacrylamide gel (20 μg per sample). The conditions of electrophoresis,

membrane transfer and blocking were consistent with the operations in the total protein experiment. Subsequently, the membrane was incubated overnight at 4 °C with primary antibodies: p-STAT3 (1: 1,000), HIF1A (1: 1,000) and Lamin B1 (1: 10,000). Secondary antibody incubation and detection procedures matched the total protein analysis.

Molecular docking

The 3D structures of the DGMs and GCMs of PD absorbed in the blood (PD, DPD, GPN, PN, Glu, Ara, Rha, Xyl and Api) were constructed using Chem3D software. The crystal structures of the core target proteins, PTPN2 (PDB ID: 8U0H) and HIF1A (PDB ID: 1H2K), were retrieved from the RCSB Protein Data Bank database (http://www.rcsb.org). Water molecules were removed from these protein structures, and hydrogen atoms were added using PyMOL software. Subsequently, molecular docking studies were performed with AutoDock (version 1.5.7). The docking simulations employed the Genetic Algorithm, with default run parameters, and were executed in triplicate to calculate mean binding energies and standard deviations. Finally, PyMOL software was used to visualize the docking state showing the highest binding score.

Intestinal microbiota analysis of PD on microbiome-drug interaction analysis

Intestinal contents from the ileum to the cecum of mice were aseptically collected, immediately flash-frozen in liquid nitrogen, and stored at −80 °C for subsequent analysis of microbial community composition. Total genomic DNA was extracted from microbial communities using the OMG-feces DNA Kit (Omega Bio-tek, Norcross, GA, USA) according to the manufacturer's protocol [18]. DNA concentration and purity were quantified post-extraction. The V3–V4 hypervariable regions of the bacterial 16S rRNA gene were amplified via PCR using barcoded primers 338F (5′-ACTCCTACGGGAGGCAGCAG-3′) and 806 R (5′-GGACTACHVGGGTWTCTAAT-3′), with extracted DNA serving as the template. Following library construction according to established methods, all data analyses were performed on the Majorbio Cloud Platform (https://cloud.majorbio.com). Alpha diversity indices were calculated using mothur software (http://www.mothur.org/wiki/Calculators). Intergroup differences in alpha diversity were assessed using the Wilcoxon rank-sum test. Beta diversity was evaluated by Principal Coordinates Analysis (PCoA) based on Bray-Curtis distances to visualize structural similarities among microbial communities. Finally, Linear Discriminant Analysis Effect Size (LEfSe) (http://huttenhower.sph.harvard.edu/LEfSe) identified taxa exhibiting significant abundance differences (from phylum to species level) between groups.

Statistical analysis

All data are reported as the mean ± standard deviation. Comparisons between multiple groups were calculated using a one-way analysis of variance (ANOVA). Data such as histograms were generated using data analysis and plotting in GraphPad Prism version 8.0 software. Statistical significance was concluded when the p-value was < 0.05.

Results and discussion

Identified metabolites of PD

Identified DGMs in vitro and in serum

It is well known that the platycosides could be transformed by the intestinal microbiota to form DGMs after oral administration. Our previous study [19] and Lee-Fong Yau group's work [30] showed that DGMs are the main metabolites of platycosides with parent nucleus, and parts of them could enter the blood to become potential active metabolites. On the other hand, the monosaccharide linkage sequence in glycosidic chain of platycosides is always consistent. Hence, the DGMs of PD could be tentatively identified according to the stepwise loss of the monosaccharide molecules of PD and further verified by the standards. The results of the TIC of DGMs and standards are shown in Fig. 1A–B and Table 1, respectively. 10 DGMs derived from PD were successfully identified in vitro, designated as: PD-Api-Xyl, PD-Api-Xyl-Rha, DPD, PD, PD-Glu-Api-Xyl, GPN, PD-Glu-Api, PD-Glu, PD-Glu-Api-Xyl-Rha, and PN. Among the 10 identified DGMs, PD, GPN, DPD, and PN were unambiguously identified by comparison with authentic reference standards. The remaining metabolites were identified by using high-resolution accurate mass measurement and MS/MS fragmentation analysis. MS/MS spectra were assigned by characteristic neutral losses of glycosyl moieties (e.g., 162 Da for glucose, 146 Da for rhamnose). Identification was further supported by comparison with published data on PD metabolism [20]. The MS/MS spectra of the corresponding compounds and the standard substances are presented in Supplementary Material 1 (Fig. 1S for PD-Api-Xyl, Fig. 2Sfor PD-Api-Xyl-Rha, Figs. 3S–5S for DPD, Figs. 6S–8S for PD, Fig. 9S-11S for GPN, Fig. 12S for PD-Glu, Fig. 13S for PD-Glu-Api-Xyl-Rha, Fig. 14S-16S for PN). The kinetic transformation results (Fig. 1C-L) showed that the concentration of PD gradually decreased, while the concentration of most DGMs slowly increased after being incubated with intestinal microbiota and then increased sharply starting at about 4–6 hours. which may be caused by the logarithmic growth phase of the intestinal microbiota, where rapid biomass expansion and peak metabolic activity

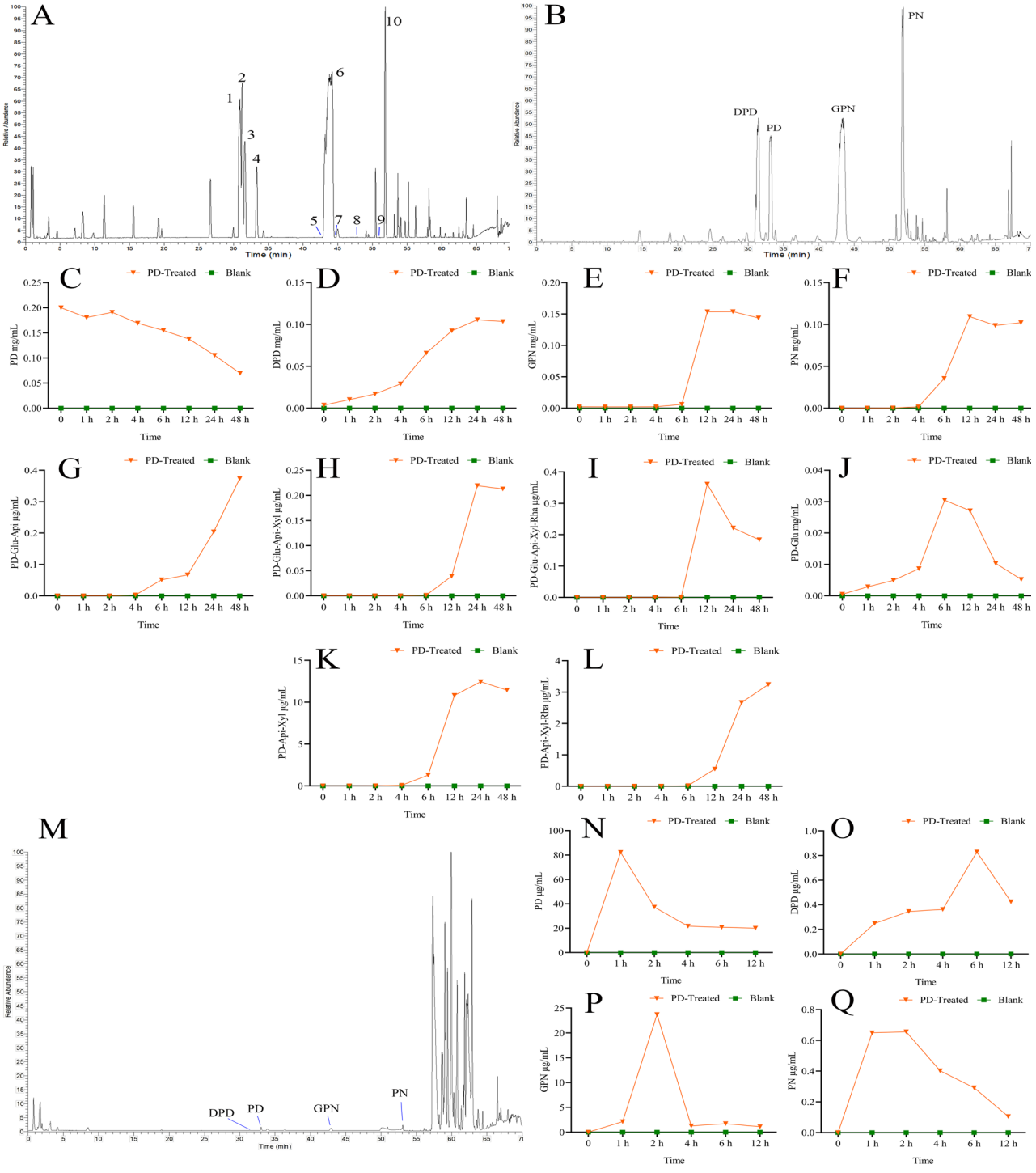

Fig. 1 Deglycosylated metabolites of PD in vitro and in serum. **A**: TIC diagram of PD deglycosylated metabolites in vitro in negative ion mode (pooled samples); **B**: TIC diagram of the platycosides mixed standard in negative ion mode; **C**-**L**: Temporal variation profile of PD deglycosylated metabolites contents in vitro, C is PD, D is DPD, E is GPN, F is PN, G is PD-Glu-Api, H is PD-Glu-Api-Xyl, I is PD-Glu-Xyl-Rha, J is PD-Glu, K is PD-Api-Xyl, L is PD-Api-Xyl-Rha. M: TIC diagram of PD deglycosylated metabolites in serum in negative ion mode (pooled samples); **N-Q**:Temporal variation profile of PD parent metabolites contents in serum, N is PD, O is DPD, P is GPN, Q is PN. PD, DPD, GPN and PN were confirmed by authentic standards, while the others were putatively identified by highresolution MS and MS/MS

Table 1 Mass spectrometry information of the deglycosylated metabolites metabolites in vitro

Peak No.	Name	Formula	RT/min	Theoretical *m/z*	Measured *m/z*	Adduct	Error/ppm	Ion fragments MS/MS
1	PD-Api-Xyl	$C_{47}H_{76}O_{20}$	30.88	959.4857	959.4849	-H	−0.85	869.4663, 820.3710, 753.4812, 723.4689, 681.6234, 663.5459, 519.4913, 457.5014, 391.4928
2	PD-Api-Xyl-Rha	$C_{41}H_{66}O_{16}$	31.23	813.4278	813.4307	-H	3.55	767.3796, 753.3267, 723.3956, 681.4091, 663.4609, 519.5156, 457.3469, 391.3535
3	DPD	$C_{52}H_{84}O_{24}$	31.65	1091.5280	1091.5287	-H	0.66	1034.5791, 1001.5294, 753.4012, 723.3582, 681.4143, 663.3994, 519.3508, 457.3406, 391.3185
4	PD	$C_{57}H_{92}O_{28}$	33.33	1223.5702	1223.5715	-H	1.03	1133.5507, 1091.5320, 753.5045, 681.4128, 519.3568, 469.3691, 457.3076, 391.3041
5	PD-Glu-Api-Xyl	$C_{41}H_{66}O_{15}$	43.23	797.4329	797.4340	-H	1.39	797.4340
6	GPN	$C_{36}H_{58}O_{12}$	43.82	681.3856	681.3864	-H	1.25	635.4417, 519.3848, 471.3601, 457.3359, 409.3442, 391.3352
7	PD-Glu-Api	$C_{46}H_{74}O_{19}$	44.26	929.4752	929.4715	-H	−3.93	929.4715
8	PD-Glu	$C_{51}H_{82}O_{23}$	47.79	1061.5174	1061.5184	-H	0.93	1043.4299, 971.4023, 591.2847, 519.2673, 469.0684, 409.0827, 391.2449
9	PD-Glu-Api-Xyl-Rha	$C_{35}H_{56}O_{11}$	50.84	651.3750	651.3756	-H	0.94	605.3601, 519.3348, 471.3390, 547.3282, 409.3443, 391.3222,
10	PN	$C_{30}H_{48}O_{7}$	51.83	519.3327	519.3334	-H	1.30	473.2908, 457.2986, 409.2971, 391.3081

accelerated PD biotransformation, corresponding to the observed surge in metabolite concentrations.

The components that enter the serum are actually the effective ones. Therefore, the DGMs of PD in the serum were analyzed. The TIC diagram of DGMs in serum is shown in Fig. 1M. Although 10 DGMs of PD were identified in vitro, only 4 of them, namely PD, DPD, GPN and PN, were found in the serum. This might be ascribed to the content of DGMs and interference of the blood, since only those with relative high content could enter and be identified in the blood with greater interference [31]. Meanwhile, the kinetic transformation results (Fig. 1N-Q) showed that the contents of these 4 metabolites entering the serum gradually increased after 1 h of oral administration of PD, which was consistent with the intestinal absorption process. Therefore, PD and the 3 DGMs detected in the blood namely DPD, GPN and PN are potential active metabolites of PD against ALI.

Identified GCMs of PD in vitro and in serum

During the deglycosylation metabolism of PD, a large number of GCMs are inevitably produced. In recent years, many GCMs like monosaccharides and oligosaccharides have shown excellent biological activity [21, 22]. Therefore, GCMs may also be the active metabolites of PD against ALI. Since the saccharide arrangement of PD is known, he GCMs of PD could be tentatively identified, and further verified by standards. And the results of GCMs and standards are shown in Fig. 2A–B and Table 2, respectively. A total of 9 GCMs were identified in vitro, including 5 monosaccharides (Glu, Ara, Rha, Xyl and Api), 3 disaccharides (Ara-Rha, Rha-Xyl and Xyl-Api), and one trisaccharide (Ara-Rha-Xyl). Ara, Glu, Api, Rha, and Xyl were confirmed by authentic standards, while the others were putatively identified by high-resolution MS and MS/MS. The identification of metabolites was verified by comparing overlayed extracted ion chromatograms (EICs) of authentic standards with those detected in samples, demonstrating co-elution and identical retention times (Supplementary Material 2, Figs. 1S–4S for Ara, Figs. 5S–8S for Xyl, Fig. 9S-12S for Api, Fig. 13S-16S for Rha, Fig. 17S-20S for Glu). The MS/MS spectra of the corresponding compounds and the standard substances are presented in Supplementary Material 1 (Fig. 17S-19S for Api, Fig. 20S-22S for Ara, Fig. 23S-25S for Rha, Fig. 26S-28S for Glu, Fig. 29S-31S for Xyl, Fig. 32S for Ara-Rha, Fig. 33S for Xyl-Api, Fig. 34S for Rha-Xyl, Fig. 35S for Ara-Rha-Xyl). The results of kinetic transformation (Fig. 2C–K) showed that the contents of Ara and Rha first decreased and then increased after 4–6 hours, which was contrary to the kinetic transformation trend of other GCMs first increasing and then decreasing. The cause of this phenomenon is still unclear, and further experimental research is needed. Obviously, the existence of disaccharides and trisaccharide and the kinetic transformation clearly showed that those oligosaccharides and monosaccharides were derived from PD, and accordingly they were also the potential active metabolites of PD. The possible reason why tetrasaccharides have not been discovered is that the hydrolysis mode of the glycosidic bond makes tetrasaccharides more prone to breakage, coupled with their very low content.

Similar to the in vitro research methods, the TIC of GCMs in serum is shown in Fig. 2L. Five GCMs in serum, namely Glu, Ara, Rha, Xyl and Api were identified, while disaccharides and trisaccharides were not detected in serum. It might be that monosaccharides have corresponding transporters and are more easily absorbed into

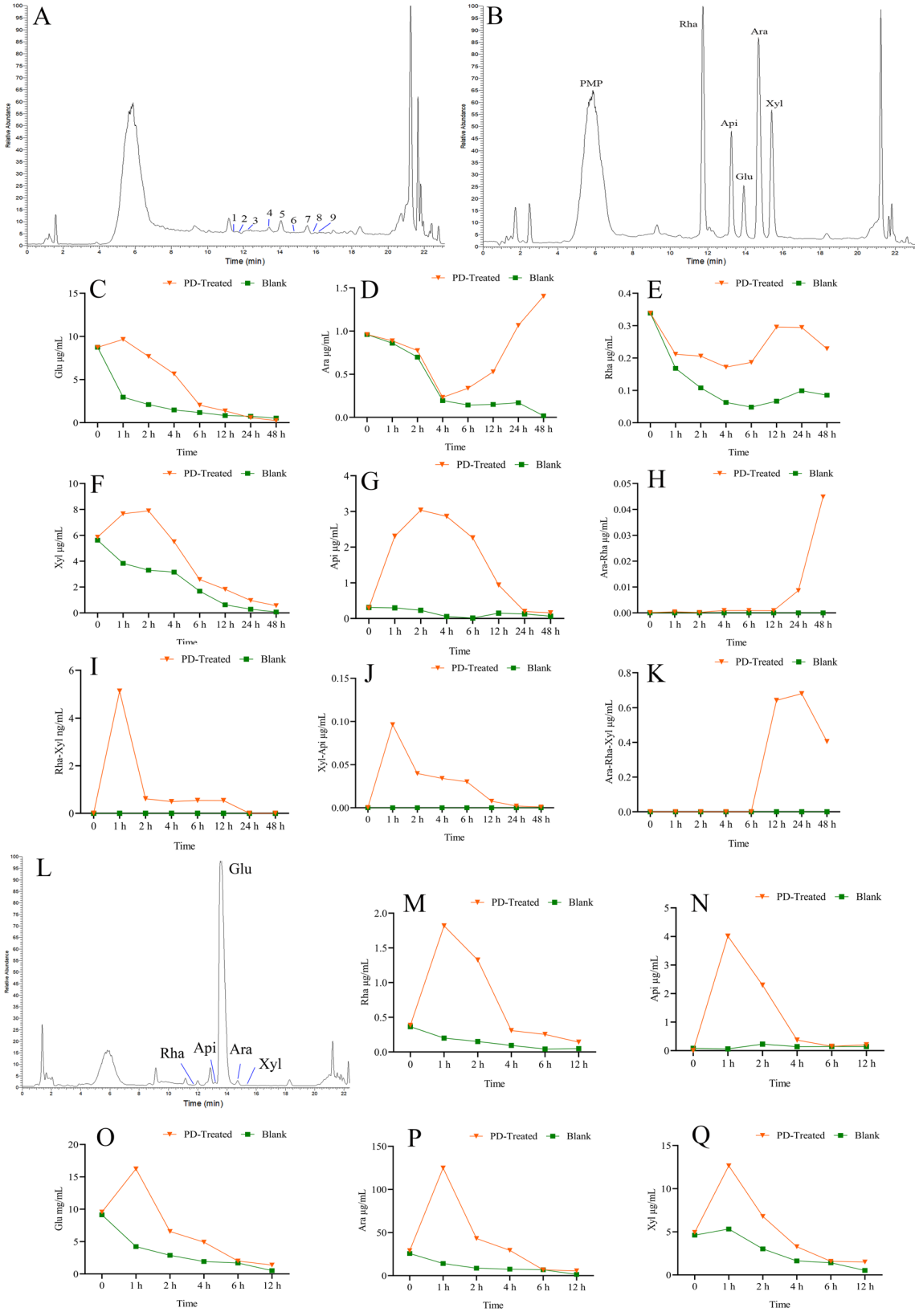

Fig. 2 (See legend on next page.)

(See figure on previous page.)

Fig. 2 Glycosidic chain metabolites of PD in vitro and in serum. **A**: TIC diagram of PD glycosidic chain metabolites in vitro in positive ion mode (pooled samples); **B**: TIC diagram of the glycosidic chain metabolites mixed standard in positive ion mode; **C**-**K**: temporal variation profile of PD glycosidic chain metabolites contents in vitro, C is Glu, D is Ara, E is Rha, F is Xyl, G is Api, H is Ara-Rha, I is Rha-Xyl, J is Xyl-Api, K is Ara-Rha-Xyl. **L**: TIC diagram of PD glycosidic chain metabolites in serum in positive ion model (pooled samples); **M-Q**: temporal variation profile of PD glycosidic chain metabolites contents in serum, M is Glu, N is Ara, O is Rha, P is Xyl, Q is Api. Ara, Glu, Api, Rha, and Xyl were confirmed by authentic standards, while the others were putatively identified by highresolution MS and MS/MS

the blood, while the transporters of disaccharides and trisaccharides are lacking; in addition, the disaccharides and trisaccharides may be further transformed into monosaccharides due to their low content. The results of kinetic transformation (Fig. 2M-Q) showed that contents of all five GCMs first increased and then decreased, and the peak time was about 1 hour for all. This is consistent with the absorption of DGMs. Therefore, 5 GCMs detected in the serum namely Glu, Ara, Rha, Xyl and Api may also be the active metabolites of PD.

Identification of SCFAs metabolites of PD in vitro and in serum

The metabolism of PD generates a large amount of GCMs, which are important precursor substances for the synthesis of SCFAs [24]. Hence SCFAs may also be active metabolites of PD worthy of analysis. All SCFAs were unambiguously identified using authentic reference standards. The identification results of SCFAs are shown in Fig. 3A–B and Table 3. The MS/MS spectra of the corresponding compounds and the standard substances are presented in Supplementary Material 1 (Fig. 36S-37S for acetic acid, Fig. 38S-39S for propionic acid, Fig. 40S-41S for isobutyric acid, Fig. 42S-43S for butyric acid, Fig. 44S-45S for 2-methylbutanoic acid, Fig. 46S-47S for isovaleric acid, Fig. 48S-49S for valeric acid, Fig. 50S-51S for hexanoic acid). A total of 8 SCFAs were identified in vitro, namely acetic acid, propionic acid, isobutyric acid, butyric acid, 2-methylbutyric acid, isovaleric acid, valeric acid and hexanoic acid. The kinetic transformation results (Fig. 3C-J) showed that although the content of SCFAs in the medium given PD increased, the rate of increase was lower than that in the blank medium, indicating that PD inhibited the production of SCFAs. The possible reason is that there are abundant glycosidic bonds in the glycosidic chain of PD. When the energy generated by the hydrolysis of glycosidic bonds in PD meets the metabolic needs of the intestinal microorganisms, only GCMs are produced. Regrettably, since the content of SCFAs in the serum is inherently low and PD shows an inhibitory effect on the production of SCFAs in the intestine, SCFAs have not been detected in the body. Therefore, the results showed that SCFAs are not the active metabolites of PD.

Bioinformatics analysis

Targets of PD metabolites in serum

As mentioned above, 4 DGMs of PD, DPD, GPN, PN and 5 GCMs of Glu, Ara, Rha, Xyl, and Api were identified as potential active forms of PD. Thus, those metabolites were applied to predict the possible targets. The SDF structures of these components were uploaded to Swiss Target Prediction, Pharmmapper and Super-PRED databases for target prediction. The targets with a probability greater than 0 obtained from the Swiss Target Prediction platform, targets with a probability greater than 50% in the Super-PRED database, and the targets with Norm Fit values greater than 0.7 in the Pharmmapper platform were considered potential targets for the metabolites of PD. The targets collected from the three databases were normalized through the UniProt database (https://www.uniprot.org/id-mapping) and the duplicate values were removed. Finally, 295 potential targets of DGMs and 251 potential targets of GCMs were collected.

Dataset acquisition and DEGs analysis of ALI

In order to screen for ALI-related targets, GSE2411 and GSE18341 were obtained from the GEO database, and both of these datasets were used to induce ALI in mice with LPS. Firstly, cluster analysis on the GSE2411 and GSE18341 dataset was performed to identify and remove outliers. As shown in Figs. 4A and 5A, samples clearly segregated into normal and LPS-induced ALI groups with no outliers detected. To identify differentially expressed genes (DEGs) between control and ALI samples, the 'Limma' package in R was utilized. DEGs were selected based on the criteria of an absolute log fold change (|logFC|) >1 and an adjusted p-value < 0.05. This approach ensured the accuracy and reliability of genomic data for subsequent analyses. A total of 247 differentially expressed genes related to ALI were screened out in the GSE2411 dataset. Among them, compared with the normal control group, 227 genes were upregulated, and 20 genes were downregulated in the lung tissues of LPS-induced ALI mice (Fig. 4B). Using the same method, 366 differentially expressed genes were screened out from the GSE18341 dataset, among which 289 genes were upregulated, and 77 genes were downregulated (Fig. 5B).

WGCNA analysis of ALI

To further screen for ALI-related targets, WGCNA analysis based on GSE2411 and GSE 18,341 was conducted.

Table 2 Mass spectrometry information of the glycosidic chain metabolites in vitro

Peak No.	Name	Formula	RT/min	Theoretical m/z	Measured m/z	Adduct	Error/ppm	Ion fragments MS/MS
1	Ara-Rha	$C_{31}H_{38}N_4O_{10}$	11.32	627.2661	627.2689	+H	4.51	628.2814, 609.2109, 495.6383, 479.7009, 375.0267, 322.0186, 286.8740, 175.8260
2	Rha	$C_{26}H_{30}N_4O_6$	11.72	495.2238	495.2260	+H	4.42	477.1323, 373.0992, 321.0850, 285.0562, 241.0388, 217.0369, 175.0417
3	Xyl-Api	$C_{30}H_{36}N_4O_{10}$	12.19	613.2504	613.2529	+H	4.04	614.2056, 481.4253, 464.3600, 374.1053, 308.0207, 272.2025, 175.7920
4	Api	$C_{25}H_{28}N_4O_6$	13.29	481.2082	481.2069	+H	−2.62	482.1260, 463.1244, 373.1105, 307.0800, 289.0720, 271.0668, 259.0730, 217.0673, 175.0931
5	Glu	$C_{26}H_{30}N_4O_7$	13.98	511.2187	511.2174	+H	−2.59	493.1363, 373.1269, 337.0666, 271.0513, 241.0403, 217.0422, 175.0391
6	Ara	$C_{25}H_{28}N_4O_6$	14.82	481.2082	481.2066	+H	−3.24	463.1710, 373.1256, 307.0650, 289.0555, 241.0516, 217.0531, 175.0470
7	Xyl	$C_{25}H_{28}N_4O_6$	15.45	481.2082	481.2068	+H	−2.83	481.1922, 471.4333, 463.1635, 307.0888, 289.0731, 271.0785, 241.0661, 217.0680, 175.0760
8	Rha-Xyl	$C_{31}H_{38}N_4O_{10}$	15.72	627.2661	627.2686	+H	4.03	628.2715, 609.2418, 481.6125, 375.2120, 271.9984, 242.1408, 187.7904, 175.1448
9	Ara-Rha-Xyl	$C_{36}H_{46}N_4O_{14}$	16.00	759.3083	759.3104	+H	2.73	759.8086, 627.5035, 614.1371, 482.1086, 374.4559, 308.2997, 242.9112

In WGCNA analysis, the soft-thresholding power $\beta = 7$ was first determined to ensure scale-free topology (Fig. 4C) of GSE2411 and $\beta = 9$ was determined (Fig. 5F). The expression matrix was consecutively transformed into an adjacency matrix and subsequently into a topological overlap matrix (TOM). Using average linkage hierarchical clustering based on TOM dissimilarity, gene modules were identified through the dynamic tree-cutting algorithm with a minimum module size of 100 genes. Following module detection, eigengenes were calculated for each module. Modules with highly correlated eigengenes were merged, yielding 12 distinct co-expression modules for GSE 2411 (Fig. 4D) and 13 modules for GSE18341 (Fig. 5D). The grey module contained genes not assigned to other modules. The modules with significant correlation to ALI were blue, pink, and light green (Fig. 4E), and the GS versus MM scatter diagram of the three modules is shown in Fig. 4F. Among the genes of these three key modules, a total of 354 hub genes were determined according to the criteria of GS > 0.9 and MM > 0.9. Three modules, the blue, light green and orange modules in GSE 18341 were most closely related to ALI (Fig. 5F), and the GS-MM scatter diagram of these three modules are shown in Fig. 4L. Among the genes of these three key modules, a total of 213 hub genes were identified based on the criteria of GS > 0.9 and MM > 0.9. By taking the intersection of the WGCNA genes obtained from the analysis of GSE2411 and GSE18341 with the differentially expressed genes, a total of 56 hub targets related to ALI from these two datasets were screened out (Fig. 5G).

The anti-ALI targets of PD

The 56 hub targets related to ALI were intersected with the targets of DGMs and GCMs through Venn diagrams to obtain the anti-ALI targets of these active metabolites. The results (Fig. 6A–B) showed that the DGMs could target PTPN2, and GCMs could target PTPN2 and HIF1A to exert anti-ALI effects. KEGG analysis combined with literature research was used to explain the biological functions of PTPN2 and HIF1A. On the one hand, KEGG pathway analysis (Fig. 6C–D) revealed that PTPN2 can exert an anti-ALI effect by negatively regulating the EGFR/JAK/STAT3 pathway [32–36], and HIF1A is an important target for treatment of pulmonary inflammation and acute respiratory distress syndrome (ARDS) [37–39]. On the other hand, PTPN2 can exert an anti-ALI effect by negatively regulating STAT3 levels and reducing the activation of HIF1A by STAT3 [40]. Therefore, those targets were subsequently analyzed.

Experimental verification of the anti-ALI effect and mechanism of PD

Pathological analysis of lung tissue

To verify the anti-ALI activity of PD and the mechanism of action of its metabolites, an LPS-induced ALI mouse model and a pseudo-sterile mouse model were established. Dosing regimens were determined based on literature review and preliminary experiments, with minor adjustments [41]. Histopathological examination (H&E staining) of lung tissues is presented in Fig. 7A. Compared to the control group, LPS challenge induced severe pathological alterations, including alveolar collapse, inflammatory cell infiltration, and alveolar wall thickening. All PD treatment groups demonstrated

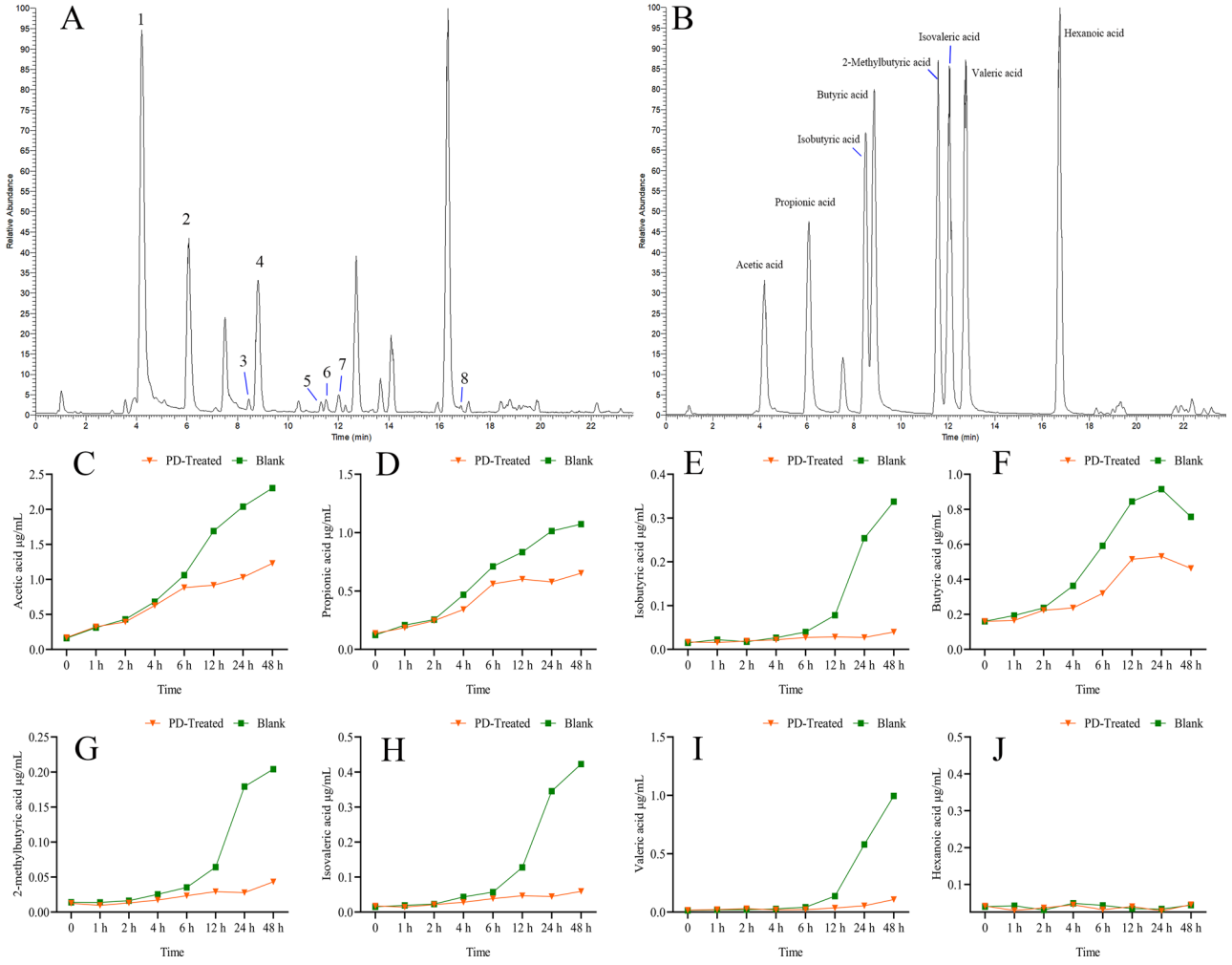

Fig. 3 SCFAs metabolites of PD in vitro. **A**: TIC diagram of PD SCFAs metabolites in vitro in negative ion mode (pooled samples); **B**: TIC diagram of the SCFAs mixed standard in negative ion mode; **C-J**: temporal variation profile of PD SCFAs metabolites contents in vitro, C is acetic acid, D is propionic acid, E is butyric acid, F is isobutyric acid, G is 2-methylbutyric acid, H is isovaleric acid, I is valeric acid, J is hexanoic acid. All SCFAs were unambiguously identified using authentic reference standards

amelioration of these pathological changes. Lung injury scores were significantly reduced in the PD-L, PD-M, and PD-H groups compared to the LPS group (Fig. 7B). Intriguingly, depletion of intestinal microbiota via oral broad-spectrum antibiotics abrogated the protective effects; both the Abs and Abs + PD-H groups showed no significant improvement in lung pathology. This indicates that the ameliorative effect of PD on lung tissue damage is dependent on intestinal microorganisms, indicating that the metabolites were the active forms of PD exerting anti-ALI effects.

Analysis of lung W/D ratio

The lung wet/dry (W/D) weight ratio, a key quantitative indicator of pulmonary edema severity, was significantly elevated in the LPS model group (Fig. 7C). All PD treatment groups significantly reduced this ratio. Consistent with the histological findings, PD failed to reduce the W/D ratio following microbiota depletion.

Biochemical index measurement

Total leukocytes in BALF were quantified, with results presented in Fig. 7D. The model group exhibited a significant increase in BALF leukocyte count, indicating intensified pulmonary inflammatory responses and aggravated alveolar damage. In contrast, all PD groups showed markedly reduced leukocyte infiltration. These results demonstrate that PD effectively attenuates LPS-induced lung inflammation and tissue injury. However, following intestinal microbiota depletion, PD failed to suppress the LPS-driven elevation of BALF leukocytes.

Furthermore, LPS challenge significantly elevated BALF and serum levels of proinflammatory cytokines IL-6, IL-1β, and TNF-α compared to the control group (Fig. 7E–G). PD treatment at various doses significantly

Table 3 Mass spectrometry information of the short chain fatty acids in vitro

Peak No.	name	Formula	RT/min	Theoretical *m/z*	Measured m/z	Adduct	Error/ppm	Ion fragments MS/MS
1	Acetic acid	$C_8H_9N_3O_3$	4.22	194.0560	194.0568	-H	4.03	194.0020, 178.0713, 151.0828, 147.0638, 137.0544, 122.1217, 106.1662
2	Propionic acid	$C_9H_{11}N_3O_3$	6.12	208.0717	208.0724	-H	3.52	208.0961, 190.0514, 178.9789, 165.0703, 152.0523, 150.0849, 137.0350, 123.0426, 106.1071
3	Isobutyric acid	$C_{10}H_{13}N_3O_3$	8.49	222.0873	222.0880	-H	3.07	222.1656, 204.0480, 192.1392, 179.1149, 164.1677, 151.0576, 137.0414, 132.1135, 121.1573, 108.1084
4	Butyric acid	$C_{10}H_{13}N_3O_3$	8.82	222.0873	222.0881	-H	3.52	222.1288, 204.0591, 194.0485, 179.0761, 175.0899, 164.0658, 151.0696, 137.0449, 122.0892, 106.1190
5	2-Methyl-butanoic acid	$C_{11}H_{15}N_3O_3$	11.48	236.1030	236.1038	-H	3.52	236.1227, 221.1564, 218.0889, 207.2082, 193.1149, 189.1195, 178.0673, 165.0782, 152.0615, 137.0279, 122.1249, 107.1707
6	Isovaleric acid	$C_{11}H_{15}N_3O_3$	11.95	236.1030	236.1035	-H	2.25	236.1122, 218.1220, 207.0282, 193.1311, 178.0997, 164.1064, 137.1507, 122.2639, 106.2777
7	Valeric acid	$C_{11}H_{15}N_3O_3$	12.68	236.1030	236.1038	-H	3.52	236.1002, 218.0898, 206.0315, 193.1293, 189.1298, 178.0678, 164.0671, 152.0700, 145.9957, 137.0686, 122.0828, 106.1684
8	Hexanoic acid	$C_{12}H_{17}N_3O_3$	16.74	250.1186	250.1191	-H	1.93	250.1449, 232.0871, 206.1152, 191.0565, 188.1197, 176.0827, 165.1079, 152.0747, 137.0711, 122.1505, 112.1287, 106.1601

downregulated these cytokine levels. Crucially, after microbiota depletion with Abs, no significant differences in serum or BALF levels of IL-6, IL-1β, and TNF-α were observed between the Abs, Abs-PD-H, and LPS model groups (Fig. 7H–J). These results demonstrate that orally administered PD exerts a dose-dependent therapeutic effect against LPS-induced ALI in mice. However, its anti-ALI activity is critically dependent on the presence of functional intestinal microbiota. This strongly suggests that PD itself is likely not the direct bioactive form responsible for these effects.

Western blotting analysis

To verify the potential mechanism of PD in the treatment of ALI, Western blotting was performed to detect the expression of the above proteins. The results are shown in Fig. 8A–E. Compared with the normal group, the protein expression level of PTPN2 was significantly decreased ($p < 0.05$) and the protein expression level of HIF1A in the LPS group of mice was significantly increased. Similarly, the expressions of p-EGFR/EGFR, p-JAK1/JAK1, and p-STAT3/STAT3 were significantly increased in LPS group. After PD administration, the expression level of PTPN2 increased significantly ($p < 0.05$) and the level of HIF1A decreased significantly ($p < 0.05$). Meanwhile, the levels of p-EGFR/EGFR, p-JAK1/JAK1, and p-STAT3/STAT3 were also significantly decreased in each PD group. However, there was no significant difference in expression levels between the Abs group and the Abs+PD-H group. This indicated that after oral administration of the mixed antibiotics, which killed the intestinal microbiota, PD was unable to regulate these proteins.

HIF1A and p-STAT3 are transcription factors that need to enter the cell nucleus to function. Therefore, the expression levels of these two proteins in nuclear proteins should be detected. The results are shown in Fig. 8F–G. The protein contents of HIF1A and p-STAT3 in the nucleus of mice in the model group increased, while each PD administration group could down-regulate the levels of HIF1A and p-STAT3 in the nuclei. Similarly, after oral administration of the mixed antibiotics, PD did not show regulatory effects on these two proteins. This indicated that PD may exert an anti-ALI effect by regulating PTPN2, HIF1A and their upstream and downstream proteins. Moreover, the regulation of these proteins by PD depends on the action of intestinal microbiota. It is further explained that the DGMs (GPN, PN) and GCMs (Glu, Ara, Rha, Xyl, and Api) of PD are its actual effective forms.

Molecular docking analysis

To further investigate the interactions between metabolites (PD, DPD, GPN, PN, Glu, Ara, Rha, Xyl and Api) and direct targets (PTPN2 and HIF1A) and thereby screen out the active metabolites of PD, molecular docking was performed. The results of the binding energy of DGMs and GCMs with PTPN2 and HIF1A are shown in Table 4. The results were analyzed and visualized through PyMOL software, as shown in Fig. 9. It can be seen from Fig. 9and Table 4 that the DGMs and GCMs mainly bind to these core targets through hydrogen bonds, van der Waals forces and electrostatic forces. On the one hand, a lower binding energy always shows a stronger binding affinity and higher activity, and when the binding

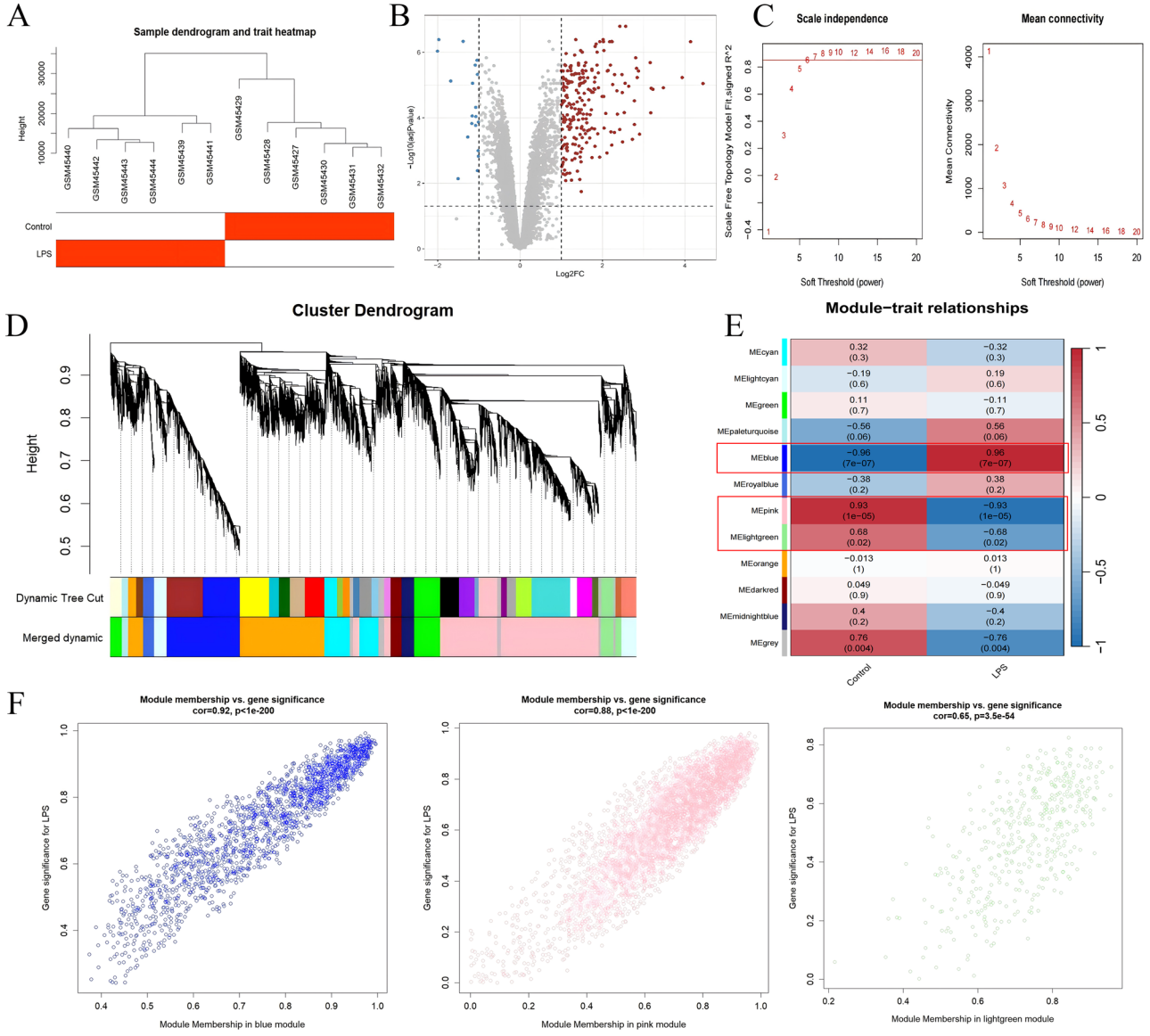

Fig. 4 Screen of hub genes related to the ALI of GSE2411 dataset. **A**: The sample dendrogram and trait heatmap. **B**: Volcano plot of differential gene analysis. blue dots indicate down-regulation, red dots indicate up-regulation, grey dots indicate no significant difference; **C**: Scale-free fitting index (left) and average connectivity (right) of various soft threshold power β. The red line represents the correlation coefficient; **D**: The clustering dendrogram of co-expressed genes of GSE2411 dataset; **I**-**J**: Heatmap of the correlation between the module eigengenes and exposure to LPS of GSE2411 dataset. **F**: Gene significance verses module membership (GS-MM) scatter diagram of the GSE2411 dataset

energy is less than 0 indicates that the ligand molecule can spontaneously bind to the receptor molecule [42, 43]. As shown in Table 4, the binding energy of PD to the PTPN2 target is greater than 0, indicating that PD is difficult to bind to PTPN2, and the binding energy of DPD to PTPN2 is close to 0. Therefore, this clearly indicates that there is only low affinity between them. The binding energies of GCMs with PTPN2 and HIF1A are shown in Table 4. It can be found that the binding energies of all GCMs with PTPN2 and HIF1A are all less than 0, indicating that GCMs can spontaneously bind to these targets. Hence, molecular docking results showed that the DGMs of GPN, PN and GCMs of Glu, Ara, Rha, Xyl, and Api were the active metabolites of PD.

Modulatory effect on intestinal microbiota of PD

To verify the bidirectional interaction bwteen PD and intestinal microbiota, 16S ribosomal RNA (16S rRNA) analysis was also performed. For 16S rRNA sequencing, the generated sequences were clustered at a 97% operational taxonomic unit (OTU) similarity level and chimeras were removed. After the number of all sample sequences was drawn flat to 20,000, OTU taxonomic annotation was performed, and the community

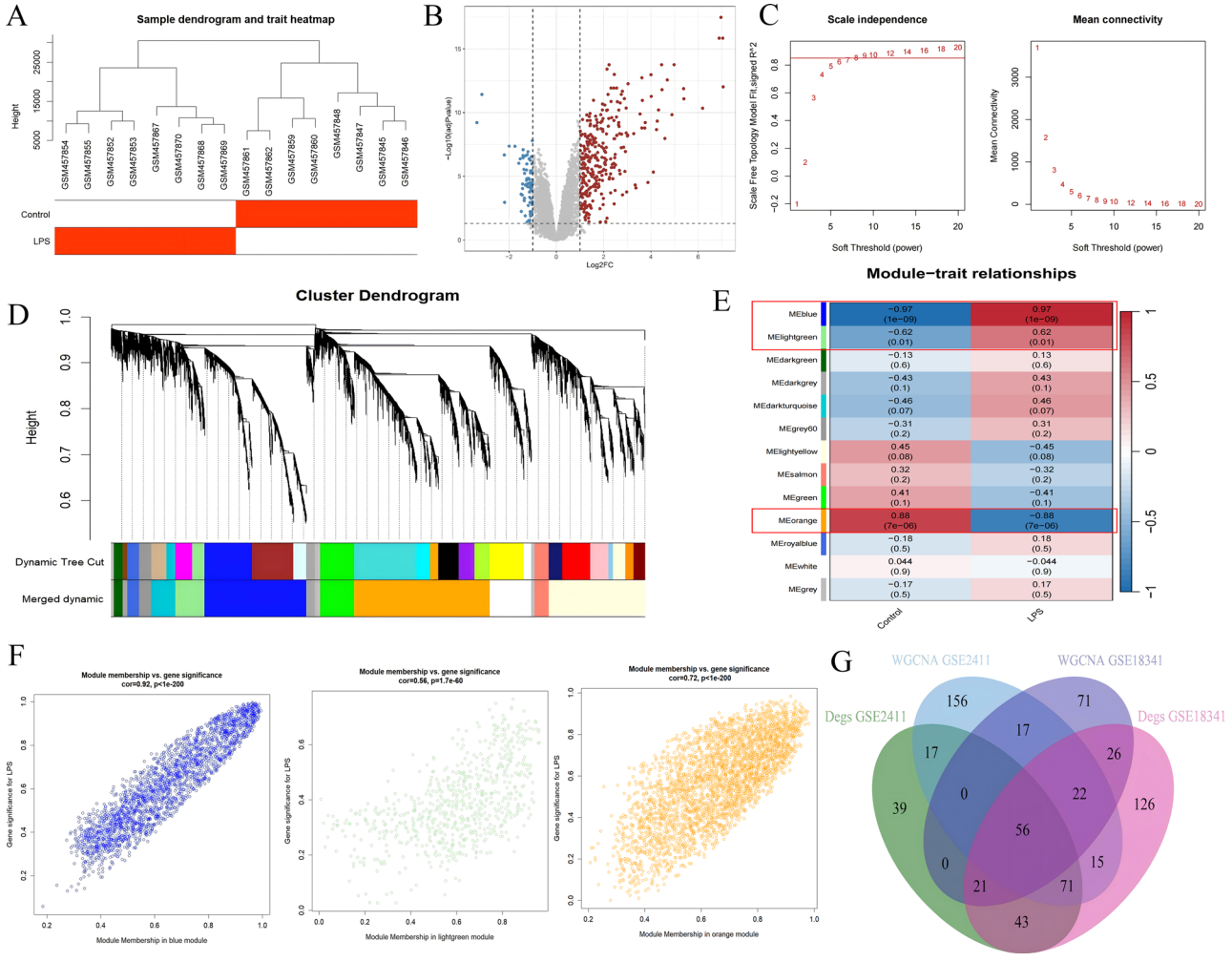

Fig. 5 Screen of hub genes related to the ALI of GSE18341 dataset. **A**: The sample dendrogram and trait heatmap. **B**: Volcano plot of differential gene analysis. Blue dots indicate down-regulation, red dots indicate up-regulation, grey dots indicate no significant difference; **C**: Scale-free fitting index (left) and average connectivity (right) of various soft threshold power β of GSE18341 dataset. The red line represents the correlation coefficient; **D**: The clustering dendrogram of co-expressed genes of GSE18341 dataset; **E**: Heatmap of the correlation between the module eigengenes and exposure to LPS of GSE18341 dataset. **F**: Gene significance verses module membership (GS-MM) scatter diagram of the GSE18341. **G**: Venn diagram of candidate differentially expressed genes following the intersection of an essential co-expression module gene and differentially expressed genes from GSE2411 and GSE18341 dataset

composition of each sample was statistically analyzed at different species classification levels. The Sobs and Shannon diversity scarcity curves tend to flatten, indicating that the amount of sequence data is suitable for reasonably representing the community (Fig. 10A–B). The α diversity of the microbiota in the Abs and Abs+PDH groups of mice decreased, indicating a reduction in species diversity. Their material diversity was significantly lower than that of the other groups, suggesting that the pseudo-sterile mouse model was successful and the mixed antibiotics successfully killed the intestinal bacteria of the mice (Fig. 10C–D). Typing analysis of PCoA and Partial Least Squares Discriminant Analysis (PLS-DA) at the OTU level showed that samples in each group could be significantly distinguished, and samples in the same group could cluster together, indicating that PD treatment changed the microbiota structure, and the PD-H group was more similar to the control group (Fig. 10E–F). In addition, the heatmaps and Circos analyses of 5 groups of bacteria and observed changes in the composition and function of the microbial community after PD treatment were examined (Fig. 10G–H).

Figure 10I-K shows the intestinal microbiota groups with significant differences among different groups of mice. The ratio of Bacteroidetes to Firmicutes in the intestinal microbiota metabolism affects the host metabolism [9]. Based on microbiome analysis at the phylum level, it can be found that Bacteroides and Firmicutes were the most common bacteria in the intestinal microbiota of each group of mice (Fig. 10J). The content of

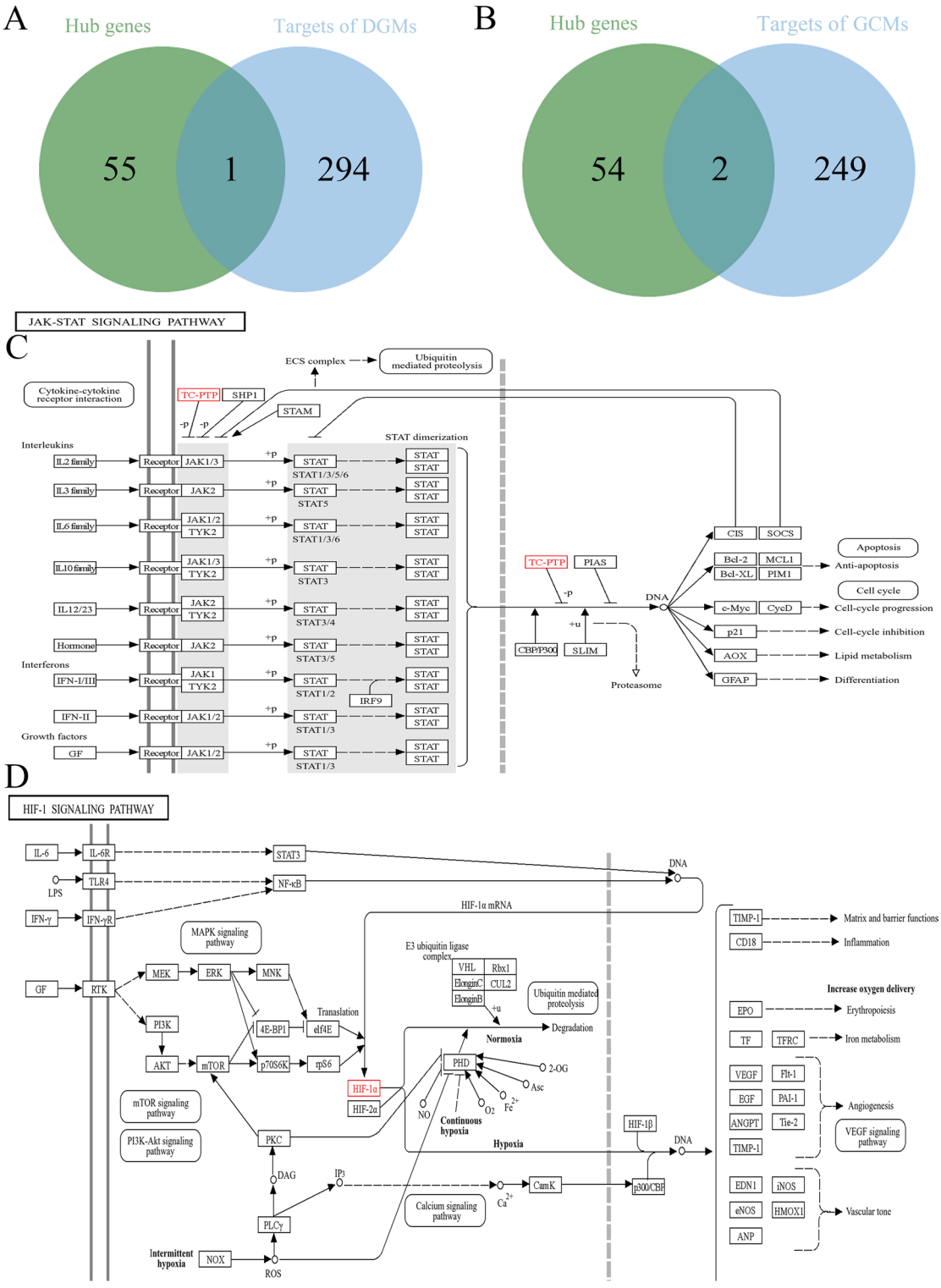

Fig. 6 Screen the core genes of PD's anti-ALI effect. **A**: Venn plot of the intersection of the target gene of PD nuclear metabolites and 56 hub genes in the GSE2411 and GSE18341 datasets. The overlapped target is PTPN2. **B**: Venn plot of the intersection of the target gene of PD glycosidic chain metabolites and 56 hub genes in the GSE2411 and GSE18341 datasets. The overlapped targets are PTPN2 and HIF1A. **C**: Signal pathway map of PTPN2 involved in ALI. **D**: Signal pathway map of HI1F1A involved in ALI. Note: TC-PTP is T-cell protein tyrosine phosphatase, and PTPN2 is the name of the gene encoding this protein

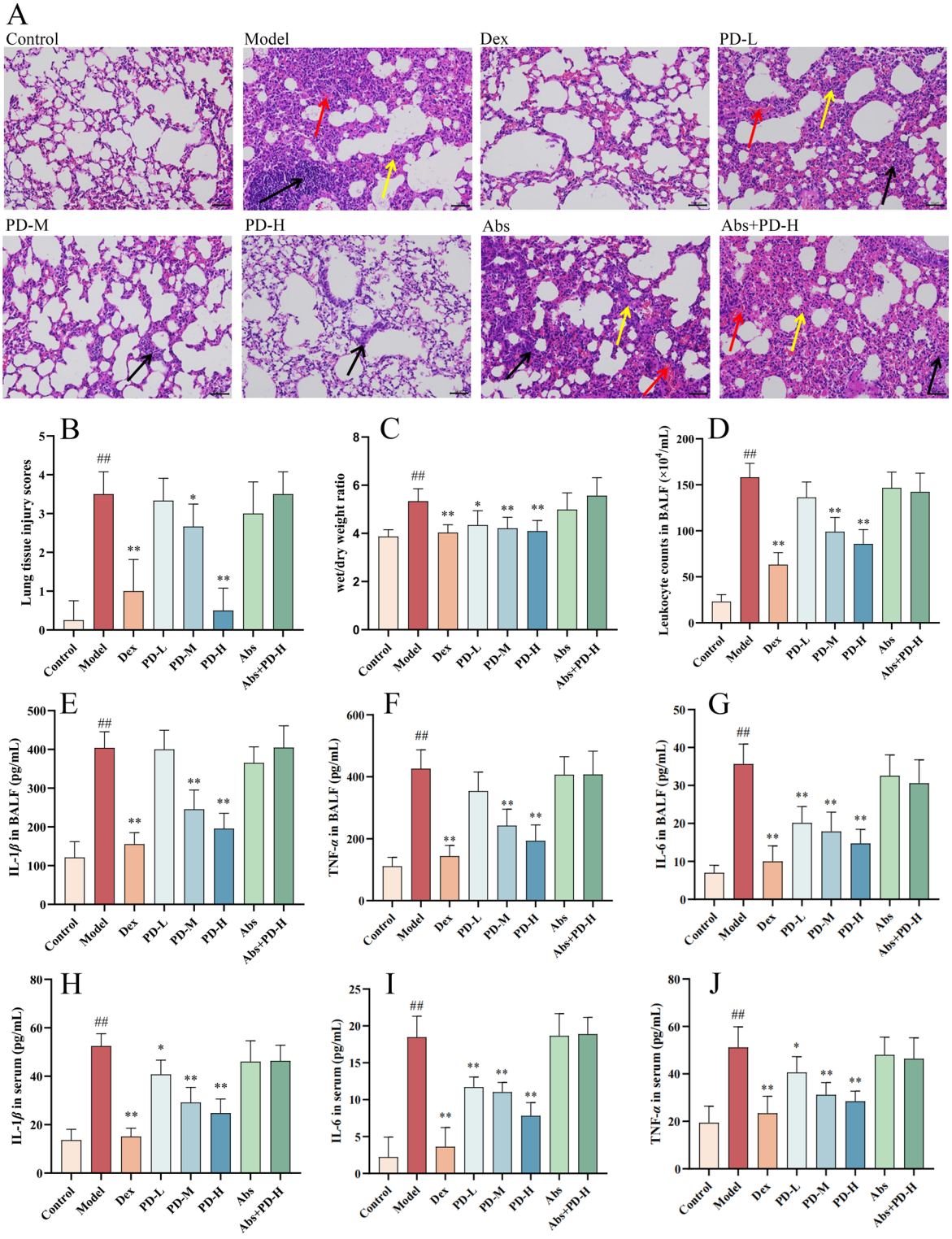

Fig. 7 PD alleviated lung injury and inflammation in LPS-induced ALI mice. **A**: Histopathological examination of lung sections through H&E staining (200×). Red arrow: pulmonary hemorrhage; yellow arrow: alveolar wall thickening; black arrow: inflammatory cell infiltration; **B**: Lung injury scores ($n = 3$, mean ± SD); **C**: Lung wet/dry weight ratio ($n = 10$, mean ± SD). **D**: Leukocyte counts in BALF ($n = 10$, mean ± SD). **E**-**G**: IL1-β (E), TNF-α (F), and IL-6 (G) contents in BALF ($n = 10$, mean ± SD). **H**-**J**: IL-1β (H), IL-6 (I), and TNF-α (J) contents in serum ($n = 10$, mean ± SD). $^{\#\#}p < 0.01$ vs normal group; $^{*}p < 0.05$, $^{**}p < 0.01$ vs model group

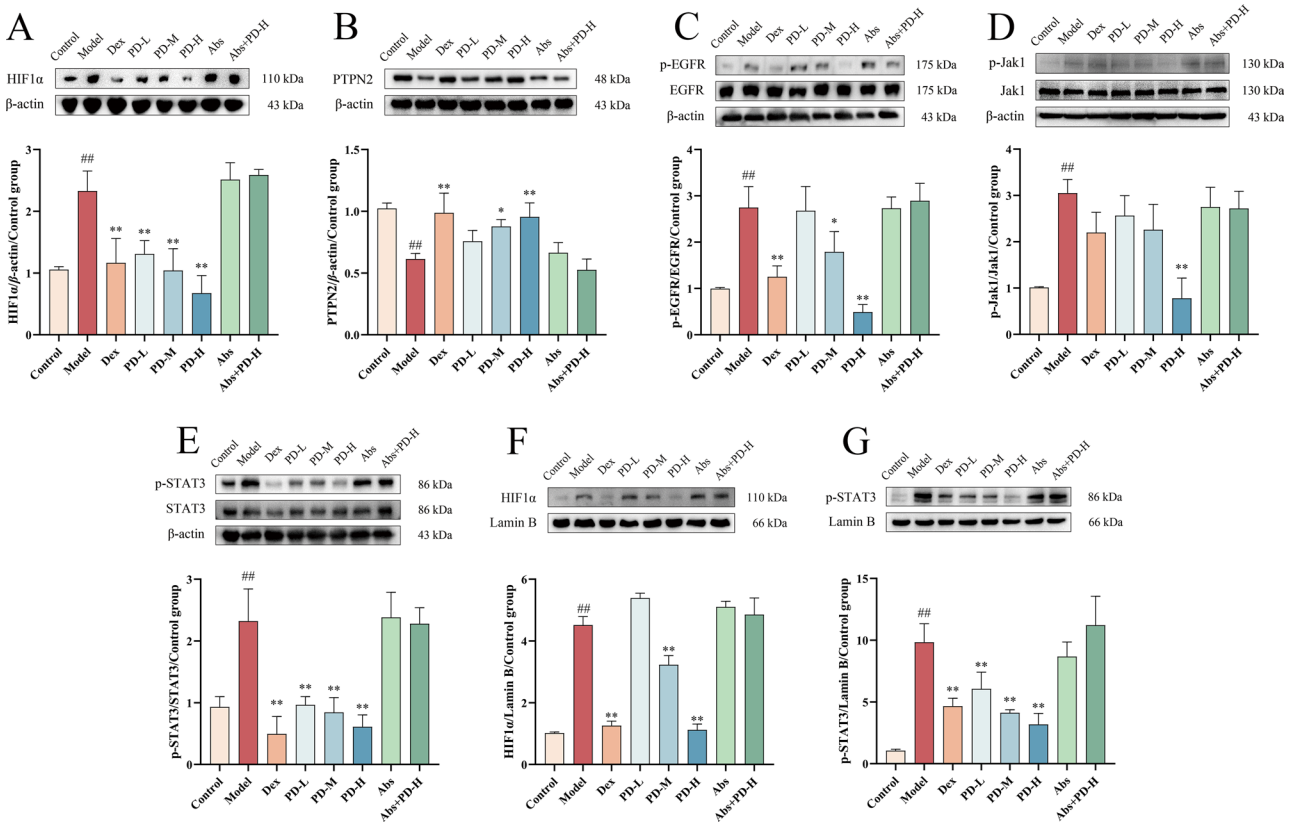

Fig. 8 Effects of PD on expression of proteins related to ALI in lung of mice. **A**-**E**: The expression levels of HIF1A (**A**), PTPN2 (**B**), p-EGFR/EGFR (**C**), p-Jak1/Jak1 (**D**) and p-Stat3/Stat3 (**E**) in the total protein of mice lung; **F**-**G**: The expression levels of HIF1A (**F**) and p-Stat3 (**G**) in the nucleoprotein of mice lung. ($n = 3$, mean ± SD), $^{\#\#}p < 0.01$ vs normal group; $^{*}p < 0.05$, $^{**}p < 0.01$ vs model group

Table 4 Molecular docking results of components and targets

Target	Ligand	Binding energy (kcal/mol)	vdw_hb_desolv Energy (kcal/mol)	Electrostatic energy (kcal/mol)	Binding site
PTPN2	Glu	−4.34	−4.57	−0.66	ASP-182, PHE-183, SER-217, ALA-218, GLY-219, ILE-220, GLY-221, ARG-222
	Ara	−4.65	−5.12	−0.72	ASP-182, PHE-183, SER-217, GLY-221, ARG-222
	Rha	−5.06	−5.98	−0.21	ASP-182, PHE-183, ALA-218, ARG-222, GLN-264
	Xyl	−4.30	−5.18	−0.31	ASP-182, PHE-183, SER-217, ALA-218, ARG-222
	Api	−4.33	−5.07	−0.74	ASP-182, PHE-183, ALA-218, ARG-222
	PD	3.25	−6.23	−0.06	GLU-11, ARG-16
	DPD	0.41	−7.57	−0.07	SER-82, PRO-207
	GPN	−5.40	−9.54	−0.34	ASN-27, ASP-50, ARG-252, GLY-257
	PN	−6.35	−8.51	−0.20	ASM-63, GLU-65, GLU-138, ASN-163
HIF1A	Glu	−3.05	−4.68	−0.16	THR-302, TYR-798
	Ara	−4.07	−4.91	−0.35	ASN-171, LEU-182, GLU-816, ARG-820
	Rha	−4.37	−5.22	−0.34	GLN-174, LEU-182, GLU-816
	Xyl	−4.34	−5.02	−0.52	ASN-171, GLN-174, LEU-182, GLU-816, ARG-820
	Api	−4.39	−4.96	−0.92	TYR-102, ARG-238, GLU-801, VAL-802, ALA-804

Bacteroidetes increased in the model group mice, while that of Firmicutes decreased in the model group. The levels of Bacteroidetes and Firmicutes in each PD administration group tended to those of the control group. As shown in Fig. 10K, analysis of differences at the genus level revealed that high-dose PD significantly decreased the abundance of intestinal microbiota genera such as Muribaculum, Eubacterium ventriosum, norank_f_Desulfovibrionaceae and Parabacteroides, while significantly increasing the abundance of genera such as no

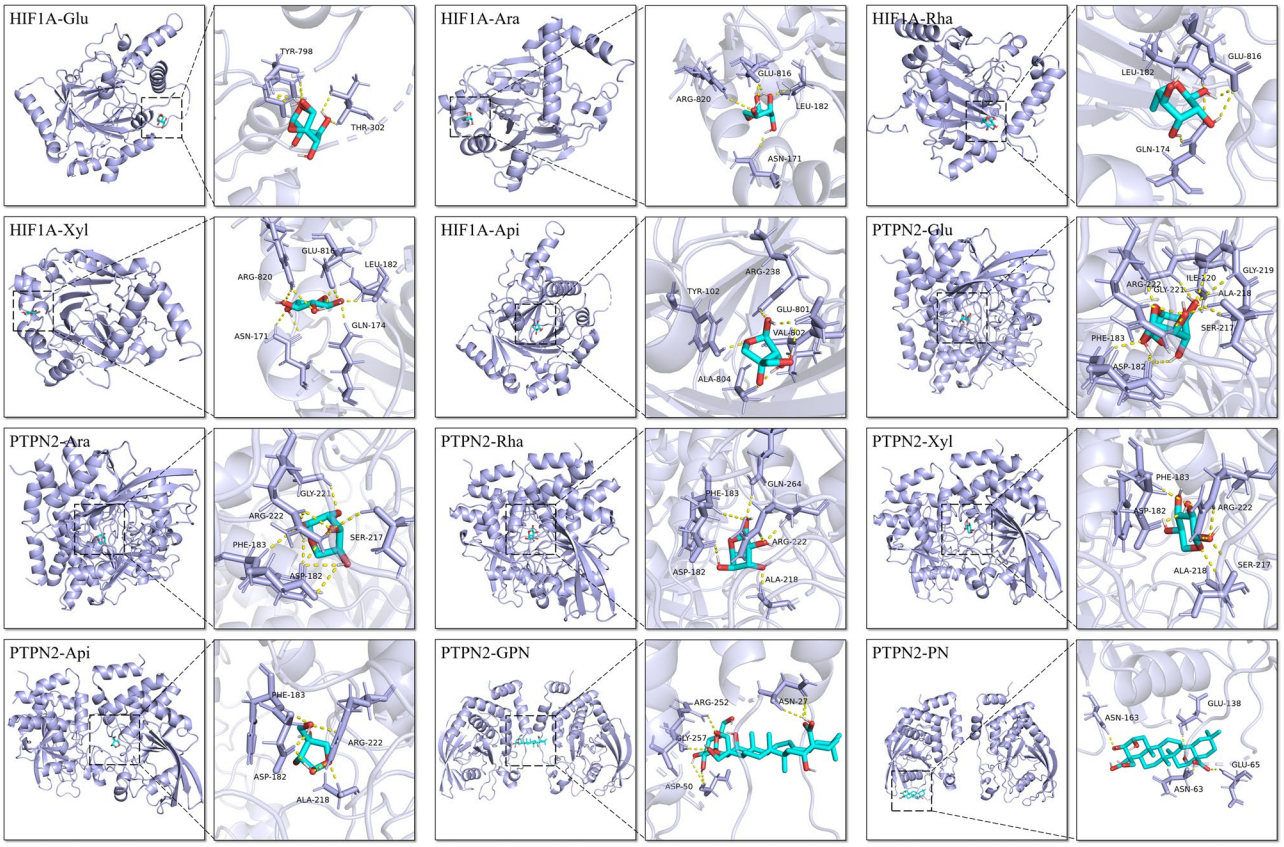

Fig. 9 The 3D interaction diagrams of deglycosylated metabolites of PD and glycosidic chain metabolites of PD with HIF1A and PTPN2

rank_f_Eubacterium coprostanoligenes group, Acetatifactor, Acetitomaculum, and norank_f_Peptococcaceae.

Studies have shown that Muribaculum bacteria can have a significant impact on T cells, and the cardiolipin they produce can strongly induce the production of pro-inflammatory cytokines such as TNF-α, IL-6 and IL-23 [44]. norank_f_Desulfovibrionaceae is a type of Desulfovibrionaceae bacteria. An increase in its abundance is often regarded as a signal of intestinal flora imbalance, and these bacteria often have pro-inflammatory effects [45]. no rank_f_Eubacterium coprostanoligenes group is a type of Eubacterium coprostanoligenes that can alleviate chemotherapy-induced intestinal mucositis by enhancing intestinal mucus barrier [46]. These findings indicate that PD not only takes effect by directly acting on the targets through its active metabolites, but also can reduce the content of some pathogenic bacteria and increase the content of some probiotics, thereby influencing its anti-ALI effect.

Exploring the metabolic transformation and mechanisms of PD in treating ALI

PD is a typical triterpenoid saponin known for its anti-ALI effects. However, its structural characteristics result in extremely poor oral bioavailability [15], making it challenging to exert its effects in prototype form [19, 20]. These limitations, at least partially, account for the unclear activities and mechanisms of PD in treating ALI, thereby severely hindering its potential for further drug development. Microbiome-drug interaction analysis is a new field that reveals the metabolites and modulatory effects of natural products on intestinal microbiota. It is reported that platycosides could be metabolized by the intestinal microbiota into various metabolites, including deglycosylated, hydroxylated, dehydroxylated, methylated, decarboxylated, acetylated, dehydrogenated, and glucuronidated forms, among others [19, 30]. Notably these studies also revealed that the DGMs of platycosides are the main intestinal metabolites, as the abundance of other metabolites is relatively low. Particularly, DGMs are the metabolites whose structures can be accurately identified. Thus, it is reasonable to focus on studying the activities and mechanisms of DGMs of PD.

Integrating microbiota-drug interaction analysis, bioinformatics, and experimental validation to uncover the anti-ALI mechanisms of PD

It is reasonable to assume that the deglycosylation of PD may inevitably generate GCMs of oligosaccharides, monosaccharides, and/or SCFAs, during

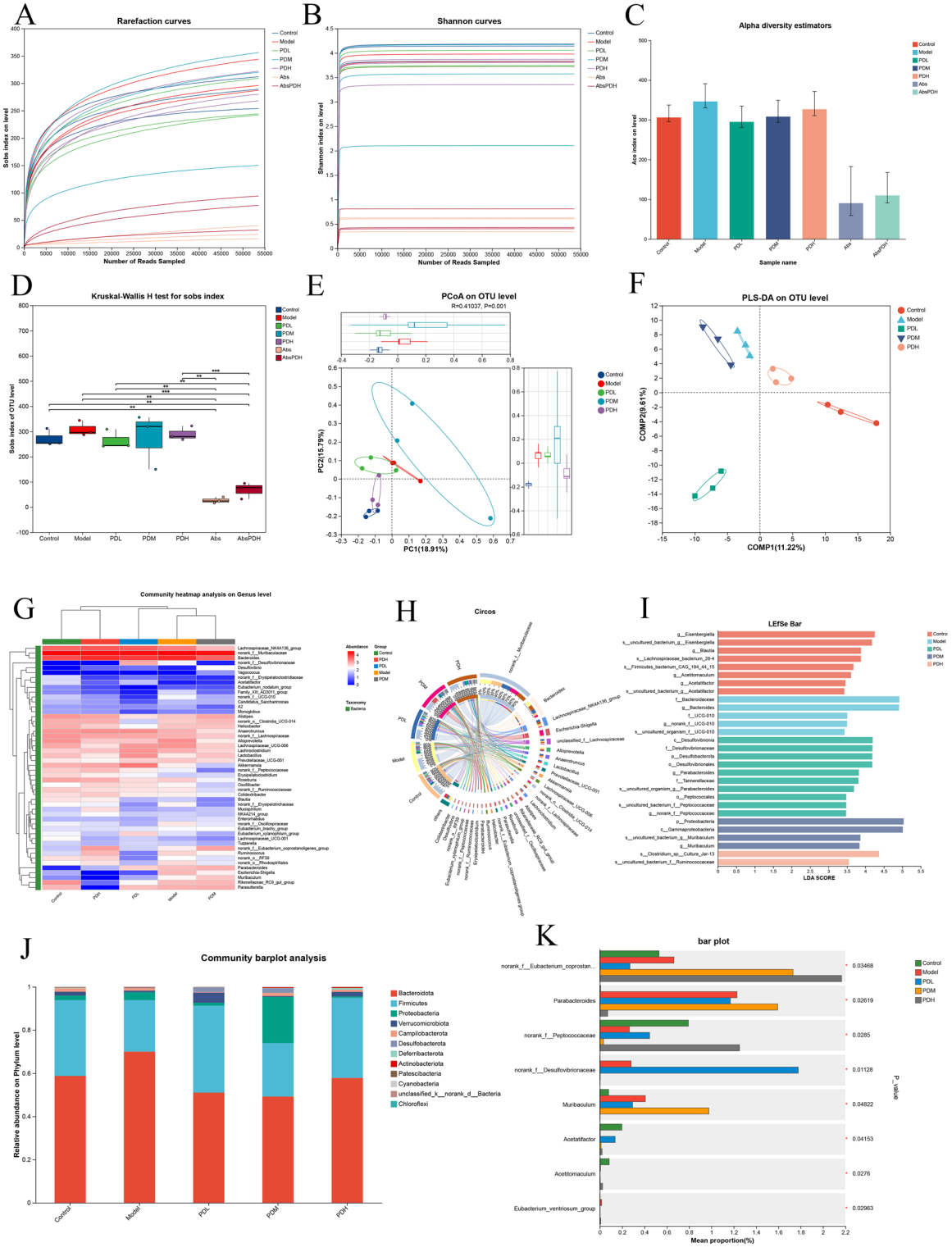

Fig. 10 Intestinal microbiota diversity analysis. **A**-**B**: Rarefaction curve calculated indexes of sobs, and Shannon on OTU level; **C**: Alpha diversity estimators calculated indexes of Shannon on OTU level; **D**: Statistical differences among groups were evaluated using the Kruskal-Wallis H test for sobs index; **E**-**F**: PCoA and PLS-DA analyses on the OTU level; **G**: Community heatmap analysis revealing variation of microbial community composition and function on genus level; **H**: Circos plots depicting the relationships between the samples and species of intestinal microbiota; **I**: Linear discriminant analysis coupled with effect size measurements identifies significant abundance; **J**: Community Bar plot analysis showed the percent of community abundance on phylum level; **K**: Statistical differences among five groups were evaluated using the Kruskal-Wallis H test on genus level ($^{*}p < 0.05$)

microbiota-drug interactions [47]. The high activities of oligosaccharides and monosaccharides as well as SCFAs implied their activities and mechanisms are also worthy of investigation [21, 22, 24]. Furthermore, the bioinformatics method for gene screening based on the gene chip data of real clinical samples in the GEO database, significantly reduces false positives compared with traditional methods, it significantly reduces false positives compared to traditional methods, making it particularly well-suited for elucidating the complex, multi-target mechanisms of natural-product metabolites and discovering new targets [13, 14]. Hence, an integrated approach combining microbiota-drug interaction, bioinformatics analysis and experimental validation provides a unique advantage in clarifying the anti-ALI activities and mechanisms of PD.

Unveiling the metabolic pathways of PD: insights into the role of DGMs, GCMs, and the inhibition of SCFAs transformation

The results showed that besides the modulatory effects on intestinal microbiota, both DGMs and GCMs of PD could be identified in vitro and in serum through microbiota-drug interaction analysis; Conversely, the transformation of saccharides to SCFAs was significantly inhibited in both in vitro and serum conditions, which is inconsistent with previous reports [47]. This novel phenomenon is very interesting, as it reveals new metabolites in the form of GCMs derived from PD and, for the first time, establishes that SCFAs are not active metabolites of PD. We speculate that the reason why the transformation of SCFAs was inhibited may be attributed to the existence of the abundant glycosidic bonds in glycosidic chain of PD. When the energy produced by the glycosidic bond hydrolysis in PD meets the metabolic needs of intestinal microbiota, only GCMs are produced. On the contrary, when the energy produced by the glycosidic bond hydrolysis is insufficient for microbial metabolic demands, these GCMs of PD may undergo further conversion to SCFAs [47].

Experimental and bioinformatics insights into the active metabolites of PD and their dual targeting of PTPN2 and HIF1A

The subsequent LPS-induced and pseudo-sterile ALI mouse models verified these findings, demonstrating that the active forms of PD are both its DGMs and GCMs, since PD showed no anti-ALI effects in LPS induced and pseudo-sterile ALI mice. In addition, the bioinformatics method WGCNA, which is based on the gene chip data of real clinical samples in the GEO database for gene screening, can reflect the essential characteristics and patterns of diseases reliably, accurately and efficiently. It is widely used in the search for new drug targets [48]. In this work, the bioinformatics analysis combined with experimental validation verified for the first time that DGMs could target PTPN2, whereas GCMs could target not only PTPN2 but also HIF1A. Molecular docking results showed the active metabolites were DGMs of GPN and PN, GCMs of Glu, Ara, Rha, Xyl and Api. These findings are consistent with previous studies, which reported that GPN and PN are the active metabolites of PD with hepatoprotective activities [19], while Rha is an active metabolite exhibiting anti-ARDS activity [23]. Interestingly, the discovery that GCMs can target the two targets further highlights the significant activities of GCMs.

Elucidating the roles of PTPN2 and HIF1A in the anti-ALI mechanisms of PD metabolites

On the other hand, the reason that only 2 targets were discovered in this work may be attributed to the bioinformatics analysis based on WGCNA, which uses the actual experimental data and significantly reduces false positives compared to traditional methods [13, 14]. Importantly, our findings are highly meaningful as they reveal, for the first time, that the anti-ALI bioactivities of PD extend beyond its parent nucleus metabolites. Specifically, GCMs exhibit high activities, whereas SCFAs are not necessarily active metabolites of glycosides, despite their saccharide-rich structures.

The biological function analysis of the targets using bioinformatics further demonstrated that PTPN2 and HIF1A play crucial roles in the treatment of ALI. Tyrosine-protein phosphatase non-receptor type 2 (PTPN2) is a non-receptor tyrosine-specific phosphatase that dephosphorylates receptor protein tyrosine, including epidermal growth factor receptor (EGFR), the JAK family, and the STATs family kinases, therefore exerting a series of anti-inflammatory effects [32–34]. The activation of the EGFR/JAK/STAT pathway can enhance persistent inflammation, such as that in ALI, by increasing the production of inflammatory factors and enhancing cellular responses to these factors. PTPN2 can inhibit the activation of this pathway, thus resulting in alleviating ALI [35, 36].

Hypoxia-inducible factor 1 A (HIF1A) is a major transcription factor responsible for the body's adaptation to hypoxia and an important target regulating gene expression in angiogenesis, erythropoiesis, energy metabolism and cell survival under hypoxic conditions [49]. Under lung injury conditions, HIF1A induces glycolysis and promotes cytokine release, such as TNF-α, IL-6, and IL-1β, intensifying the inflammatory response and deteriorating lung damage [37, 38]. Meanwhile, the activation of PTPN2 can negatively regulate the STAT3 pathway, which in turn alleviates the activation of HIF1A by STAT3 [40].

Advancing anti-ALI drug development: targeting PTPN2 and HIF1A through PD metabolites

This study clearly demonstrated that HIF1A and PTPN2 are new targets of PD, and numerous studies have highlighted their significant roles in ALI [39, 50]. PD's ability to regulate PTPN2 and HIF1A through its metabolites underscores that new metabolites often reveal novel mechanisms of natural products, which could be revealed by the innovative method integrating microbiome-drug interaction analysis, bioinformatics approaches and experimental validation.

In addition, taking the unique advantage of multi-target and multi-component approaches in the treatment of ALI into account, this work provides a novel strategy for developing new anti-ALI medicines. By combining different active metabolites of DGMs, GCMs, and PD, which act through distinct target mechanisms, a more effective therapeutic approach may be achieved. Hence, this work not only revealed the active DGMs and GCMs and their targets involved in the anti-ALI effects of PD but also provides novel strategies for developing new anti-ALI medicines. These strategies have the potential to significantly advance the research and enhance the resource utilization of natural products with low oral bioavailability in the development of new anti-ALI medicines [8–10].

Limitations of this study

This study has several limitations. First, the in vitro microbiota–PD biotransformation assay was conducted using fecal microbiota collected from LPS-induced ALI mice, without a parallel non-LPS healthy microbiota control incubated with PD. Therefore, while we characterized PD-derived metabolites generated under ALI-associated microbiota conditions, we could not directly quantify how ALI status alters PD biotransformation relative to baseline microbiota. Future studies will incorporate matched healthy controls to assess disease-associated shifts in microbiota-driven metabolism of PD. Second, Sex is a biologically relevant variable in ALI and in host–microbiota interactions. Because only male mice were used, sex-dependent differences in immune responses and microbiota composition/metabolic capacity may influence PD biotransformation and treatment outcomes. Future studies incorporating female cohorts are warranted to assess the generalizability and potential sex-specificity of the metabolite profile and PTPN2/HIF1A-related mechanisms.

Conclusions

This study reveals previously uncharacterized active DGM and GCM metabolites of Platycodin D (PD) and implicates PTPN2 and HIF1A as key mechanistic targets through an integrated workflow combining microbiome-drug interaction analysis, bioinformatics, and experimental validation. The bioactivity of glycosides extends beyond parent nucleus metabolites, as GCMs derived from the glycosidic chain also possess high activity. SCFAs are not necessarily active metabolites of glycosides despite their saccharides-rich structures in this context. In addition, this study establishes a new paradigm for elucidating active metabolites and mechanisms of natural products, especially glycosides with low oral bioavailability, advancing natural product research and ALI treatment strategies. The activities of the metabolites will be addressed in subsequent studies.

Subsequent studies will focus on further validating the PTPN2/HIF1A regulatory mechanism of PD metabolites, identifying PD-metabolizing intestinal microbiota, exploring the tissue distribution and synergistic effects of active metabolites, and developing multi-component composite preparations. These studies will provide a theoretical basis for the clinical transformation of PD and its active metabolites, and offer novel strategies for ALI therapy.

Abbreviations

16S rRNA	16S ribosomal RNA
3-NPH	3-nitrophenylhydrazine
ALI	Acute lung injury
Abs	Mixed antibiotics group
Abs+PD-H	Mixed antibiotics and high dosage platycodin D group
ANOVA	Analysis of variance
Api	Apiose
Ara	Arabinose
ARDS	Acute respiratory distress syndrome
BALF	Bronchoalveolar lavage fluid
DEGs	Differentially expressed genes
DGMs	Deglycosylated metabolites
DPD	Deapio-platycodin D
EDC	1-ethyl-3-(3-dimethylaminopropyl) carbodiimide
EGFR	Epidermal growth factor receptor
GAM	General anaerobic medium
GCMs	Glycosidic chain metabolites
GEO	Gene Expression Omnibus
Glu	Glucose
GPN	3-O-β-D-glucopyranosyl platycodigenin
GS	Gene significance
HIF1A	Hypoxia-inducible factor 1 A
IL1β	Interleukin-1β
IL6	Interleukin-6
JAK1	Tyrosine-protein kinase JAK1
LEfSe	Linear Discriminant Analysis Effect Size
LPS	Lipopolysaccharide
MM	Module membership
MTBE	Methyl tert-butyl ether
OUT	Operational taxonomic unit
PCoA	Principal Coordinates Analysis
PD	Platycodin D
PD-H	Platycodin D high-dosage group
PD-L	Platycodin D low-dosage group
PD-M	Platycodin D medium-dosage group
p-EGFR	Phospho-epidermal growth factor receptor
p-JAK1	Phospho-tyrosine-protein kinase JAK1
PLS-DA	Partial Least Squares Discriminant Analysis
PMP	1-phenyl-3-methyl-5-pyrazolinone
PN	Platycodigenin
p-STAT3	Phospho-signal transducer and activator of transcription 3
PTPN2	Tyrosine-protein phosphatase non-receptor type 2
Rha	Rhamnose

SCFAs	Short-chain fatty acids
SDS	Sodium dodecyl sulfate
STAT3	Signal transducer and activator of transcription 3
TIC	Total ion current
TNFα	Tumor necrosis factor α
TOM	Topological overlap matrix
W/D	Lung wet/dry weight ratio
WGCNA	Weighted Gene Co-expression Network Analysis
Xyl	Xylose

Supplementary Information

The online version contains supplementary material available at https://doi.org/10.1186/s13062-026-00779-3.

Supplementary material 1

Supplementary material 2

Supplementary material 3

Author contributions

Yuanhan Zhong and Jinxiang Zeng designed the study. Yuanhan Zhong was involved in data collection. Yuanhan Zhong, Yu Peng, Liyun Wen and Guangpeng Liu performed the study on the identification of PD derived metabolite in vitro and in serum. Jinxiang Zeng supervised the experiments. Yuanhan Zhong, Bingbing Xu, Shouwen Zhang, Jinxiang Zeng, Junwei He, Yonghong Liang, Yong Feng and Huilian Huang performed the bioinformatics and molecular docking analysis. Yuanhan Zhong and Jinxiang Zeng performed experimental validations. Yuanhan Zhong, Jinxiang Zeng and Jian Liang drafted the manuscript. Jian Liang corrected the draft.

Funding

The work was supported by the National Natural Science Foundation of China (No. 82160736 and 81860685), Jiangxi University of Chinese Medicine Science and Technology Innovation Team Development Program (No. CXTD22002) and Joint Project between School and Local Area (No. Heng-20220348).

Data availability

All data generated or analyzed during this study are included in this published article and its supplementary information files. The datasets used and/or analyzed during the current study are available from the corresponding author on reasonable request.

Declarations

Ethics approval and consent to participate

All procedures complied with institutional and national guidelines for the care and use of laboratory animals and were approved by the Animal Care and Use Committee of Jiangxi University of Chinese Medicine (approval No. JZLLSC20250550).

Consent for publication

Not applicable.

Competing interests

The authors declare no competing interests.

Author details

[1]Research Center for Traditional Chinese Medicine Resources and Ethnic Minority Medicine, Jiangxi University of Chinese Medicine, 1688 Meiling Avenue, Nanchang 330004, China
[2]Jiangxi Key Laboratory for Sustainable Utilization of Chinese Medicinal Resources, Nanchang 330004, China
[3]Jiangxi Provincial Institute of Traditional Chinese Medicine, Nanchang 330046, China
[4]Library of Jiangxi University of Chinese Medicine, Nanchang 330004, China

Received: 25 January 2026 / Accepted: 7 April 2026

Published online: 15 April 2026

References

1. Butt Y, Kurdowska A, Allen TC. Acute lung injury: a clinical and molecular review. Arch Pathol Lab Med. 2016;140(4):345–50. https://doi.org/10.5858/arpa.2015-0519-RA
2. Matthay MA, Zemans RL, Zimmerman GA, Arabi YM, Beitler JR, Mercat A, et al. Acute respiratory distress syndrome. Nat Rev Dis Primers. 2019;5(1):18. https://doi.org/10.1038/s41572-019-0069-0
3. Meduri GU, Golden E, Freire AX, Taylor E, Zaman M, Carson SJ, et al. Methylprednisolone infusion in early severe ARDS. Chest. 2007;131(4):954–63. https://doi.org/10.1378/chest.06-2100
4. Selickman J, Vrettou CS, Mentzelopoulos SD, Marini JJ. COVID-19-related ARDS: key mechanistic features and treatments. JCM. 2022;11(16):4896. https://doi.org/10.3390/jcm11164896
5. Li J, Ma W, Tang Z, Li Y, Zheng R, Xie Y, et al. Macrophage-driven pathogenesis in acute lung injury/acute respiratory disease syndrome: harnessing natural products for therapeutic interventions (review). Mol Med Rep. 2024;31(1):16. https://doi.org/10.3892/mmr.2024.13381
6. Li P, Peng J, Li Y, Gong L, Lv Y, Liu H, et al. Pharmacokinetics, bioavailability, excretion and metabolism studies of Akebia saponin D in rats: causes of the ultra-low oral bioavailability and metabolic pathway. Front Pharmacol. 2021;12:621003. https://doi.org/10.3389/fphar.2021.621003
7. Leung KW, Wong A-T. Pharmacology of ginsenosides: a literature review. Chin Med. 2010;5(1):20. https://doi.org/10.1186/1749-8546-5-20
8. Fura A. Role of pharmacologically active metabolites in drug discovery and development. Drug Discov. Today Today. 2006;11(3–4):133–42. https://doi.org/10.1016/S1359-6446(05)03681-0
9. Fan X, Zhang Y, Song Y, Zhao Y, Xu Y, Guo F, et al. Compound danshen dripping pills moderate intestinal flora and the TLR4/MyD88/NF-κB signaling pathway in alleviating cognitive dysfunction in type 2 diabetic KK-Ay mice. Phytomedicine. 2023;111:154656. https://doi.org/10.1016/j.phymed.2023.154656
10. Weersma RK, Zhernakova A, Fu J. Interaction between drugs and the gut microbiome. Gut. 2020;69(8):1510–19. https://doi.org/10.1136/gutjnl-2019-320204
11. McCardle K. Shedding light on microbiome–drug interactions. Nat Comput Sci. 2023;3(7):577–7. https://doi.org/10.1038/s43588-023-00494-3
12. Qadri H, Shah AH, Almilaibary A, Mir MA. Microbiota, natural products, and human health: exploring interactions for therapeutic insights. Front Cell Infect Microbiol. 2024;14:175557. https://doi.org/10.3389/fcimb.2024.1371312
13. Zhang Y, Wei S, Zhang Q, Zhang Y, Sun C. Paris saponin VII inhibits triple-negative breast cancer by targeting the MEK/ERK/STMN1 signaling axis. Phytomedicine. 2024;130:155746. https://doi.org/10.1016/j.phymed.2024.155746
14. Zhang X, Gao H, Chen X, Liu Z, Wang H, Cui M, et al. Identification of sanguinarine as a novel antagonist for perfluorooctanoate/perfluorooctane sulfonate-induced senescence of hepatocytes: an integrated computational and experimental analysis. J Educ Chang Hazard Mater. 2024;478:135583. https://doi.org/10.1016/j.jhazmat.2024.135583
15. Ji M-Y, Bo A, Yang M, Xu J-F, Jiang L-L, Zhou B-C, et al. The pharmacological effects and health benefits of *Platycodon grandiflorus*—A Medicine Food homology species. Foods. 2020;9(2):142. https://doi.org/10.3390/foods9020142
16. Pei L, Bao Y, Ma L, Wang Q, Ye Y, Han X, et al. A sensitive method for determination of Platycodin D in rat plasma using liquid chromatography/tandem mass spectrometry and its application to a pharmacokinetic study. Planta Med. 2012;78(03):244–51. https://doi.org/10.1055/s-0031-1280372
17. Wu Y, Huang D, Wang X, Pei C, Xiao W, Wang F, et al. Suppression of NLRP3 inflammasome by Platycodin D via the TLR4/MyD88/NF-κB pathway contributes to attenuation of lipopolysaccharide induced acute lung injury in rats. Int Immunopharmacol. 2021;96:107621. https://doi.org/10.1016/j.intimp.2021.107621
18. Li TH, Qin Y, Sham PC, Lau KS, Chu K-M, Leung WK. Alterations in gastric microbiota after *H. pylori*eradication and in different histological stages of gastric carcinogenesis. Sci Rep. 2017;7(1):44935. https://doi.org/10.1038/srep44935
19. Zhong Y-H, Wu X-W, Zhang X-Y, Zhang S-W, Feng Y, Zhang X-M, et al. Intestinal microbiota-mediated serum pharmacochemistry reveals

hepatoprotective metabolites of Platycodonis Radix against APAP-induced liver injury. J Chromatogr B. 2025;1251:124395. https://doi.org/10.1016/j.jchromb.2024.124395
20. Xu W, Han S, Wang W, Luo Z, Wang X, Shi C, et al. Analysis of gut microbiota metabolites of platycodin D and activity verification. J Pharmaceut Biomed. 2024;242:116016. https://doi.org/10.1016/j.jpba.2024.116016
21. Lv Z, Song J, Xiang Y, Chen Z, Lu Z, Zhou Q, et al. Structural characterization and therapeutic effect of Alhagi honey oligosaccharide on liver fibrosis in mice. Fitoterapia. 2024;175:105974. https://doi.org/10.1016/j.fitote.2024.105974
22. Na T-Y, Kim G-H, Oh H-J, Lee M-H, Han Y-H, Kim KT, et al. The trisaccharide raffinose modulates epidermal differentiation through activation of liver X receptor. Sci Rep. 2017;7(1):43823. https://doi.org/10.1038/srep43823
23. Li D, Wei R, Zhang X, Gong S, Wan M, Wang F, et al. Gut commensal metabolite rhamnose promotes macrophages phagocytosis by activating SLC12A4 and protects against sepsis in mice. Acta Pharmaceutica Sin. B. 2024;14(7):3068–85. https://doi.org/10.1016/j.apsb.2024.03.025
24. Cheng J, Hu J, Geng F, Nie S. *Bacteroides* utilization for dietary polysaccharides and their beneficial effects on gut health. Food Sci Hum Wellness. 2022;11(5):1101–10. https://doi.org/10.1016/j.fshw.2022.04.002
25. Zhang C, Wang X, Zhong Y, Zhou L, Liang J, Zeng J, et al. Active microbial metabolites study on antitussive and expectorant effects and metabolic mechanisms of platycosides fraction of Platycodonis Radix. J Chromatogr B. 2022;1195:123171. https://doi.org/10.1016/j.jchromb.2022.123171
26. Zhang C, Liang J, Zhou L, Yuan E, Zeng J, Zhu J, et al. Components study on antitussive effect and holistic mechanism of Platycodonis Radix based on spectrum-effect relationship and metabonomics analysis. J Chromatogr B. 2021;1173:122680. https://doi.org/10.1016/j.jchromb.2021.122680
27. Fan B, Li T, Song X, Wu C, Qian C. A rapid, accurate and sensitive method for determination of monosaccharides in different varieties of *Osmanthus fragrans*lour by pre-column derivatization with HPLC-MS/MS. Int J Biol Macromolecules. 2019;125:221–31. https://doi.org/10.1016/j.ijbiomac.2018.12.033
28. Dei Cas M, Paroni R, Saccardo A, Casagni E, Arnoldi S, Gambaro V, et al. A straightforward LC-MS/MS analysis to study serum profile of short and medium chain fatty acids. J Chromatogr B. 2020;1154:122490. https://doi.org/10.1016/j.jchromb.2020.121982
29. Dong J, Song R, Shang X, Wang Y, Liu Q, Zhang Z, et al. Identification of important modules and biomarkers in tuberculosis based on WGCNA. Front Microbiol. 2024;15:1354190. https://doi.org/10.3389/fmicb.2024.1354190
30. Yau L-F, Huang H, Tong T-T, Bai L-B, Zhu G-Y, Hou Y, et al. Characterization of deglycosylated metabolites of platycosides reveals their biotransformation after oral administration. Food Chem: X. 2022;393:133383. https://doi.org/10.1016/j.foodchem.2022.133383
31. Li Y, Zhou G, Peng Y, Tu P, Li X. Screening and identification of three typical phenylethanoid glycosides metabolites from Cistanches Herba by human intestinal bacteria using UPLC/Q-TOF-MS. J Pharmaceut Biomed. 2016;118:167–76. https://doi.org/10.1016/j.jpba.2015.10.038
32. Simoncic PD, Lee-Loy A, Barber DL, Tremblay ML, McGlade CJ. The T cell protein tyrosine phosphatase is a negative regulator of janus family kinases 1 and 3. Curr Biol. 2002;12(6):446–53. https://doi.org/10.1016/S0960-9822(02)00697-8
33. Mattila E, Pellinen T, Nevo J, Vuoriluoto K, Arjonen A, Ivaska J. Negative regulation of EGFR signalling through integrin-α1β1-mediated activation of protein tyrosine phosphatase TCPTP. Nat Cell Biol. 2005;7(1):78–85. https://doi.org/10.1038/ncb1209
34. Hoeve JT, Ibarra-Sanchez MDJ, Fu Y, Zhu W, Tremblay M, David M, et al. Identification of a nuclear Stat1 protein tyrosine phosphatase. Mol Cell Biol. 2002;22(16):5662–68. https://doi.org/10.1128/MCB.22.16.5662-5668.2002
35. Zhao J, Yu H, Liu Y, Gibson SA, Yan Z, Xu X, et al. Protective effect of suppressing STAT3 activity in LPS-induced acute lung injury. Am J Physiol-Lung Cellular Mol Physiol. 2016;311(5):L868–80. https://doi.org/10.1152/ajplung.00281.2016
36. Severgnini M, Takahashi S, Tu P, Perides G, Homer RJ, Jhung JW, et al. Inhibition of the src and jak kinases protects against lipopolysaccharide-induced acute lung injury. Am J Respir Crit Care Med. 2005;171(8):858–67. https://doi.org/10.1164/rccm.200407-981OC
37. Codo AC, Davanzo GG, Monteiro LDB, de Souza GF, Muraro SP, Virgilio-da-Silva JV, et al. Elevated glucose levels favor SARS-CoV-2 infection and monocyte response through a HIF-1α/glycolysis-dependent axis. Cell Metab. 2020;32(3):437–46.e5. https://doi.org/10.1016/j.cmet.2020.07.007
38. Yeh CH, Cho W, So EC, Chu CC, Lin MC, Wang JJ, et al. Propofol inhibits lipopolysaccharide-induced lung epithelial cell injury by reducing hypoxia-inducible factor-1α expression. Br J Anaesth. 2011;106(4):590–99. https://doi.org/10.1093/bja/aer005
39. Tran TT, Eltzschig HK, Yuan X. Therapeutic targeting of hypoxia inducible factor in acute respiratory distress syndrome. J Physiol. 2024;602(21):5745–56. https://doi.org/10.1113/JP284599
40. Jiang Y, Xu Y, Zhu C, Xu G, Xu L, Rao Z, et al. STAT3 palmitoylation initiates a positive feedback loop that promotes the malignancy of hepatocellular carcinoma cells in mice. Sci Signal. 2023;16(814):eadd 2282. https://doi.org/10.1126/scisignal.add2282
41. Zhong YH, Liang J, Qin Q, Wang YJ, Peng YM, Zhang T, et al. The activities and mechanisms of intestinal microbiota metabolites of TCM herbal ingredients could be illustrated by a strategy integrating spectrum-effects, network pharmacology, metabolomics and molecular docking analysis: platycodin D as an example. Phytomedicine. 2023;115:154831. https://doi.org/10.1016/j.phymed.2023.154831
42. Gul A, Aimaiti M, Tuerxun T, Amat R, Reheman A, Zhang MF, et al. Study on the mechanism of Üstikuddus sherbiti in ischemic cerebrovascular diseases: based on network pharmacology. Evidence-Based Complementary Alternative Med. 2022;2022:1–16. https://doi.org/10.1155/2022/5581864
43. Wang Q, Duan X, Li S, Lai H, Cheng W, Ao J, et al. Active compounds screening and hepatoprotective mechanism of shuganning injection based on network pharmacology and experimental validation. Nat Prod Commun. 2022;17(9):17. https://doi.org/10.1177/1934578X221124756
44. Bang S, Shin Y-H, Ma X, Park S-M, Graham DB, Xavier RJ, et al. A cardiolipin from *Muribaculum intestinale*induces antigen-specific cytokine responses. J Am Chem Soc. 2023;145(43):23422–26. https://doi.org/10.1021/jacs.3c09734
45. Liu L, Wang H, Zhang H, Chen X, Zhang Y, Wu J, et al. Toward a deeper understanding of gut microbiome in depression: the promise of clinical applicability. Adv Sci. 2022;9(35):e2203707. https://doi.org/10.1002/advs.202203707
46. Bai D, Zhao J, Wang R, Du J, Zhou C, Gu C, et al. *Eubacterium coprostanoligenes*alleviates chemotherapy-induced intestinal mucositis by enhancing intestinal mucus barrier. Acta Pharmaceutica Sin. B. 2024;14(4):1677–92. https://doi.org/10.1016/j.apsb.2023.12.015
47. Li S, Hu J, Yao H, Geng F, Nie S. Interaction between four galactans with different structural characteristics and gut microbiota. Crit Rev Food Sci Nutr. 2023;63(19):3653–63. https://doi.org/10.1080/10408398.2021.1992605
48. Zhang S, Liu K, Liu Y, Hu X, Gu X. The role and application of bioinformatics techniques and tools in drug discovery. Front Pharmacol. 2025;16:1547131. https://doi.org/10.3389/fphar.2025.1547131
49. Liu Z, Xi R, Zhang Z, Li W, Liu Y, Jin F, et al. 4-hydroxyphenylacetic acid attenuated inflammation and edema via suppressing HIF-1α in seawater aspiration-induced lung injury in rats. IJMS. 2014;15(7):12861–84. https://doi.org/10.3390/ijms150712861
50. LaFleur MW, Nguyen TH, Coxe MA, Miller BC, Yates KB, Gillis JE, et al. PTPN2 regulates the generation of exhausted CD8+ T cell subpopulations and restrains tumor immunity. Nat Immunol. 2019;20(10):1335–47. https://doi.org/10.1038/s41590-019-0480-4

Publisher's Note